ATF6 activation alters colonic lipid metabolism causing tumor-associated microbial adaptation

Authors

Olivia I. Coleman[1] *, Adam Sorbie[1,2] *, Sandra Bierwith[1], Janine Kövilein[1], Miriam von Stern[1], Nikolai Köhler[3], Jakob Wirbel[4], Christina Schmidt[5], Tim Kacprowski[6,7,8], Andreas Dunkel[9], Josh K. Pauling[3], Johannes Plagge[10], Diego Mediel-Cuadra[11], Sophia Wagner[11], Tingying Peng[11], Thomas Metzler[12], Clemens Schafmayer[13], Sebastian Hinz[13], Christian Röder[14], Christoph Röcken[15], Bärbel Stecher[16,17], Philip Rosenstiel[18], Katja Steiger[12], Moritz Jesinghaus[19], Gerhard Liebisch[20], Josef Ecker[9], Georg Zeller[4], Klaus-Peter Janssen[21], Dirk Haller[1,22 #]

Authors' affiliation

[1] Chair of Nutrition and Immunology, School of Life Sciences, Technische Universität München, Freising-Weihenstephan, Germany.

[2] Institute for Stroke and Dementia Research (ISD), University Hospital, LMU Munich, Munich, Germany.

[3] LipiTUM, Chair of Experimental Bioinformatics, School of Life Sciences Weihenstephan, Technische Universität München, Freising-Weihenstephan, Germany.

[4] Structural and Computational Biology Unit, European Molecular Biology Laboratory, Heidelberg, Germany.

[5] Faculty of Medicine and Heidelberg University Hospital, Institute for Computational Biomedicine, Heidelberg University, Heidelberg, Germany.

[6] Division Data Science in Biomedicine, Peter L. Reichertz Institute for Medical Informatics of TU Braunschweig and Hannover Medical School, Braunschweig, Germany.

[7] Braunschweig Integrated Centre of Systems Biology (BRICS), TU Braunschweig, Braunschweig Germany.

[8] Department of Computational Biology of Infection Research, Helmholtz Centre for Infection Research (HZI), Braunschweig, Germany.

[9] Chair of Food Chemistry and Molecular Sensory Science, School of Life Sciences, Technische Universität München, Germany.

[10] Research Group Lipid Metabolism, ZIEL, Technische Universität München, Freising, Germany.

[11] Helmholtz AI, Helmholtz Munich, 85764 Neuherberg, Germany.

[12] Comparative Experimental Pathology (CEP), School of Medicine and Health, Technische Universität München, Munich, Germany.

[13] Department of General Surgery, University Hospital Rostock, Rostock, Germany.

[14] Institute for Experimental Cancer Research, University Medical Center Schleswig-Holstein, Kiel, Germany.

[15] Department of Pathology, Christian-Albrechts University, Kiel, Germany.

[16] Max von Pettenkofer Institute of Hygiene and Medical Microbiology, Ludwig-Maximilians-University of Munich, 80336 Munich, Germany

[17] German Center for Infection Research (DZIF), partner site LMU Munich, Munich Germany.

[18] Institute of Clinical Molecular Biology, University hospital Schleswig-Holstein, Campus Kiel and Kiel University, Kiel, Germany.

[19] Institute of Pathology, Universitätsklinikum Marburg, Baldingerstraße, 35043, Marburg, Germany.

[20] Institute of Clinical Chemistry and Laboratory Medicine, University Hospital Regensburg, Regensburg, Germany.

[21] Department of Surgery, Klinikum rechts der Isar, Technische Universität München, München, Germany.

[22] ZIEL Institute for Food and Health, Technische Universität München, Freising, Germany

*These authors contributed equally to this project.

[#] Corresponding author:

Prof. Dr. Dirk Haller
Technical University of Munich
Chair of Nutrition and Immunology
Gregor-Mendel-Str. 2
85354 Freising, Germany
Email: dirk.haller@tum.de
Phone: + 49 8161-71 2026

Abstract

The induction of endoplasmic reticulum unfolded protein responses (UPR^{ER}) contributes to cancer development and progression. We recently linked microbiota-related triggers to the tumor-promoting role of signal transducer activating transcription factor 6 (ATF6) in the colon. Here we substantiate the clinical relevance of ATF6 and related bacterial genera in colorectal cancer patient cohorts. Spatial and longitudinal bacterial profiling in ATF6 transgenic mice ($nATF6^{IEC}$) identified tumor-initiating and tumor-progressing shifts in the mucosa-associated microbiota. Transcriptional analysis in intestinal epithelial cells (IEC) of germ-free and specific pathogen-free $nATF6^{IEC}$ mice defined bacteria-specific changes in cellular metabolism enriched for fatty acid biosynthesis. Untargeted metabolomics, isotope-labeling in intestinal organoids and FASN inhibition confirmed ATF6-mediated involvement of long-chain fatty acids in tumorigenesis. Multi-omics data integration identified a bacteria-lipid network characterized by fatty acid efflux, catabolism and detoxification. We postulate chronic ATF6 signaling to drive a clinically relevant pathologic response altering lipid metabolism to select for a tumor-promoting microbiota.

Keywords: Activating transcription factor 6 (ATF6), intestinal epithelial cells (IEC), colorectal cancer, metabolomics, lipid metabolism, microbiota

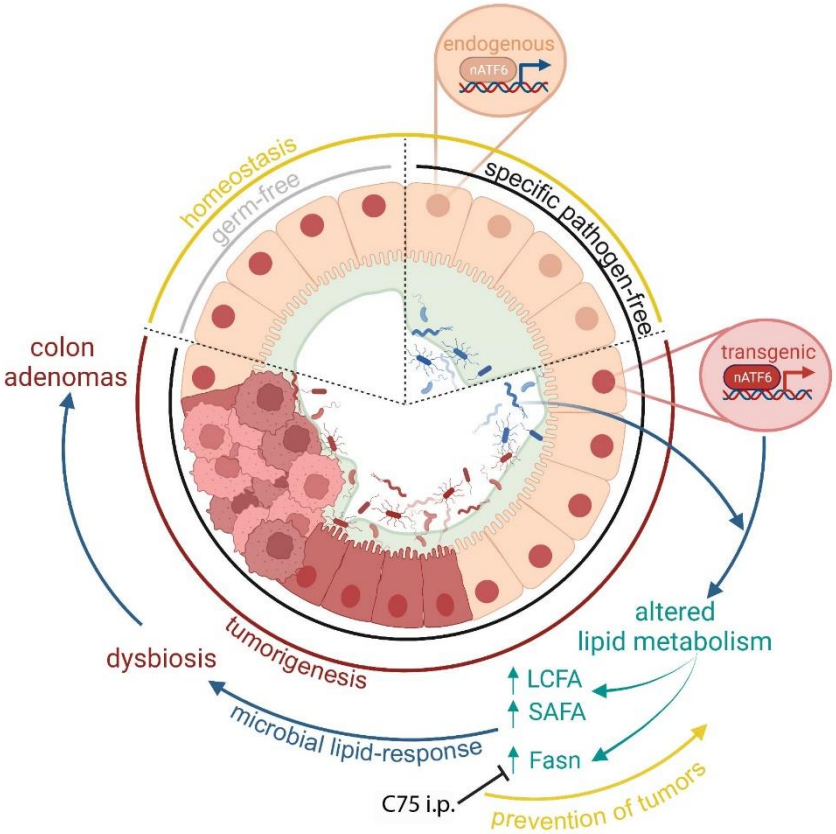

Graphical Abstract: Chronic ATF6 signaling in the colonic epithelium alters lipid metabolism to select a tumor-promoting microbiota

- nATF6 expression is induced in intestinal epithelial cells in transgenic mice (nATF6^{IEC})
- Biallelic nATF6^{IEC} germ-free mice (grey circle) and floxed or monoallelic specific pathogen-free mice (black circle) remain in a state of homeostasis (yellow circle), while biallelic specific pathogen-free mice (black circle) develop spontaneous colon tumorigenesis (red circle)
- Mechanistically, biallelic nATF6^{IEC} mice in the presence of an intestinal microbiota alter colonic lipid metabolism, including the upregulation of Fasn
- The microbial lipid-response to the altered lipid milieu results in dysbiosis and the subsequent formation of colon adenomas
- Inhibition of FASN in biallelic nATF6^{IEC} mice prevents colon tumor formation (yellow arrow)

Created with BioRender.com

nATF6: activated activating transcription factor 6; LCFA: long-chain fatty acids; SAFA: saturated fatty acids; Fasn: fatty acid synthase; C75 i.p.: intraperitoneal injection of the Fasn inhibitor C75.

Introduction

The endoplasmic reticulum (ER) in mammalian cells forms an extensive tubular-reticular network that acts as a gatekeeper controlling the synthesis and folding of proteins, and the synthesis of cellular lipids [1,2]. The accumulation of un- and misfolded ER proteins activates the unfolded protein response (UPR^{ER}), a highly conserved group of intricately regulated intracellular signaling pathways that aims to restore ER homeostasis. PKR-like ER kinase (PERK), inositol-requiring enzyme 1 (IRE1) and activating transcription factor 6 (ATF6) constitute the three main arms of the UPR^{ER} [3]. ER-stress results in the dissociation of membrane-bound ATF6 from the ER chaperone glucose-regulating protein 78 (GRP78), subsequent cleavage by the site-1 and site-2 proteases in the Golgi apparatus, and translocation of the active cytosolic N-terminal portion of the transcription factor (nATF6) into the nucleus to bind the ER-stress response element (ERSE) [4,5].

Numerous studies recognize the UPR^{ER} as a fundamental mediator in cellular physiology and the pathogenesis of inflammatory disorders, metabolic diseases and cancer, including colorectal cancer (CRC) [6-12]. Enhanced expression of GRP78, a downstream target of nATF6, correlates with growth, invasion and metastasis of tumors [13]. Furthermore, ATF6 mRNA expression and polymorphisms are associated with CRC metastasis and relapse [14,15], and hepatocellular carcinoma [16], respectively. Hanaoka *et al.* proposed ATF6 as a marker for early dysplastic changes in ulcerative colitis (UC)-associated and non-UC associated CRC [10]. In line with this, we could show that chronic transgenic expression of nATF6 specifically in intestinal epithelial cells (IECs) induces spontaneous and microbiota-dependent colon adenoma formation in a murine model of early-onset CRC ($nATF6^{IEC}$) [11]. Accumulating evidence unarguably renders the intestinal microbiota as an important regulator of host health and a causal player in the development and progression of CRC. Our findings that dysbiosis precedes tumorigenesis in $nATF6^{IEC}$ mice and that nATF6-expressing germ-free mice remain tumor-free [11], clearly indicate a mechanistic link between ATF6 signaling and the intestinal microbiota in the context of colon tumorigenesis. What remains to be elucidated, is how ATF6 signaling induces dysbiosis at the pre-tumor stage.

Alterations in the lipidomic profile have been observed in numerous cancer types [17-19], including CRC [20], which marks lipid metabolic rewiring as a phenotypic hallmark of cancer. Upregulation of fatty acid synthase (FASN), a key multi-enzyme complex of *de novo* lipid biosynthesis [21], is associated with aggressive disease and poor prognosis in CRC [22,23]. We recently described a robust CRC-specific lipid signature based on quantitative lipidomics in a multi-cohort and cross-center study, identifying triacylglycerol species and FASN gene expression as differential markers of cancerous tissue and bad prognosis, respectively [24]. Its intimate involvement in metabolism, particularly lipid metabolism, marks the UPR^{ER} as an important metabolic regulator. Evidence of direct regulation of lipid metabolism by ATF6 has been shown

by its ability to inhibit target gene expression of the cholesterol metabolism sterol regulatory element binding protein 2 (SREBP2), and to upregulate genes involved in fatty acid synthesis and elongation when overexpressed in different animal models [25-27]. Mechanistically, our understanding of the role of ATF6 signalling in CRC disease pathology is limited and mostly unexplored. Despite studies linking CRC to the UPR^{ER} or lipid metabolism to the UPR^{ER}, evidence for the triangular interplay between all three is sparse.

The multifaceted possibilities of physiological outcomes in response to the UPR^{ER} underlines the necessity to understand the mechanistic contribution of UPR^{ER} signaling to disease pathology. Here, we firstly set out to identify the relevance of ATF6 in CRC patient populations, and secondly to understand the consequence of ATF6 signaling on the murine host. We characterize ATF6 expression in multiple independent German CRC cohorts and link ATF6 activity to a CRC-associated microbiota. Furthermore, we demonstrate that ATF6 activation alters the intestinal lipid-milieu causing tumor-related changes in the microbiota.

Results

High ATF6 expression defines a subset of CRC patients and associates with CRC-enriched bacterial genera

We previously identified increased *ATF6* expression to be associated with reduced disease-free survival in colorectal cancer (CRC) patients [11]. To substantiate these findings, we quantified ATF6 protein expression via immunohistochemistry (IHC) staining in a German CRC patient cohort (cohort 1; *n=959*) using QuPath [28,29]. Findings show that ATF6 upregulation occurs in 38% of CRC patients that can be classed as ATF6-high in terms of their nuclear (NUC) and cytoplasmic (CYT) expression (Fig. 1a; Extended Data Fig. 1a,b). ATF6 expression was compared between the tumor-center (ATF6-TC) and the tumor invasive front (ATF6-IF), showing similar expression levels between these two localizations (data not shown), and subsequently averaged to determine the ATF6 H-score (capturing both the intensity and the percentage of stained cells) (Fig. 1a). To validate the above findings, we applied a deep learning model trained on ATF6 expression levels of CRC patient biopsy images in an independent CRC patient cohort (cohort 2; *n=50*) and tested on cohort 1 (Fig. 1b; Extended Data Fig. 1c,d). Here, we employed classification and regression algorithms to conduct an analysis of ATF6 expression levels. In line with our results, this independent classification identified 39% (classification task) and 35.9% (regression task) of CRC patients in cohort 1 as ATF6-high (Fig. 1c-e), confirming the robustness and applicability of our AI methodology. To further support our findings, we quantified ATF6 expression using QuPath in another German CRC patient cohort (cohort 3; *n=256*). Here we identified a subpopulation of 19% of CRC patients to be ATF6-high (Fig. 1f). To investigate a potentially dissimilar effect of ATF6 expression in patients with early-onset CRC (age<50; EOCRC) versus late-onset CRC (age>50; LOCRC), we quantified ATF6 expression in additional patients from cohort 3 with EOCRC (cohort 3; *n=55* EOCRC). Findings show similar expression levels in EOCRC, with 11% of patients classified as ATF6-high (Fig. 1g). Together, these results clearly demonstrate that high ATF6 expression defines a subpopulation (19-38%) of CRC patients.

Multiple lines of evidence undoubtedly link the intestinal microbiota with CRC. Recent developments in identifying microbial signatures in the publicly available The Cancer Genome Atlas (TCGA) dataset [30], allowed us to compare transcription factor activity (RNA-seq data) and microbial profiles (identified in whole-exome sequencing data from the same samples) in CRC patients. In a hypothesis-free approach, ATF6 was identified among the most significant transcription factors whose activities correlated positively with the presence of CRC-enriched genera, including *Campylobacter*, *Porphyromonas*, *Fusobacterium*, *Selonomonas* and *Desulfovibrio* (Fig. 1 h,i). Both *ATF6* activity and bacterial profiles are strongly associated with microsatellite instability (MSI) status of the cancer, which could be a potential confounding

factor, but we observed a strong correlation of the CRC-enriched genera with ATF6 activity even after correcting our association models for MSI status (Extended Data Fig. 1e).

Mucosal microbiota identifies ATF6-related changes in microbiota profiles associated with spatial separation between tumor and non-tumor tissue

In our transgenic mouse model of microbiota-dependent ATF6-driven tumorigenesis (nATF6^{IEC}), we previously established the interrelated role of the microbiota and ATF6 signaling in adenoma formation [11]. In agreement with our published findings, only biallelic nATF6^{IEC} mice (tg/tg) show a reduced survival (Fig. 2a), and develop colonic tumors with an incidence of 100% under specific pathogen-free (SPF) conditions, while controls (fl/fl) and monoallelic (tg/wt) mice, as well as germ-free (GF) tg/tg mice remain tumor-free (Fig. 2b). Having previously established that intestinal epithelial *Atf6* activation alters the cecal microbiota [11], we sought to investigate whether chronic *Atf6* activation alters luminal and the mucosa-associated microbiota in a spatial manner. Indeed, *Atf6* activation alters the mucosa-associated microbiota in the absence of tumor formation in tg/wt mice (Extended Data Fig. 2a,b). Furthermore, we observed augmented modulation of the mucosa-associated microbiota with increasing *Atf6* gene dose as shown by mean GUniFrac dissimilarity relative to control, between genotypes (Fig. 2c). GUniFrac dissimilarity also correlated positively with the expression of the downstream ATF6 target *Grp78*, while Shannon Effective diversity correlated negatively (Fig. 2d). We moreover observed a significant correlation between tumor number and Shannon Effective diversity, suggesting a link between tumor burden and diversity (Fig. 2e). To verify whether the mucosal microbiota can better classify the tumorigenic phenotype compared to the luminal microbiota, we applied machine learning models (Random forest (RF), LASSO (L1L) and Ridge regression (RR)) to both sample types. Two out of the three models trained on mucosal data achieved higher accuracy (Fig. 2f), and Precision-Recall curves confirmed that non-tumor and tumor samples can accurately be discriminated with our applied machine learning models (Extended Data Fig. 2c). Supporting the increased utility over luminal microbiota, two out of three models trained on mucosal microbiota data showed significantly higher AUC values across all leave-one-put cross validation repetitions (Extended Data Fig. 2d). Next, we sought to differentiate mucosal taxa associated with initial pathological changes induced by ATF6 from those associated with tumor presence, by analyzing microbial changes at pre-tumor (5wk) and tumor (12wk) time points. This enabled grouping of bacterial genera into those associated with early changes (EC, decrease in abundance over time), sustained changes (SC, sustained enrichment) and late changes (LC, increase in abundance over time). Using this approach, we identified Amplicon sequence variants (ASVs) classified as *Mucispirillum*, *Anaerotruncus* and Lachnospiraceae as responders to early changes, members of *Lactobacillus*, *Odoribacter*, *Bacteroides* and *Alistipes* as sustained taxa associated with

ATF6-induced changes, and *Lactobacillus*, *Bacteroides*, *Parabacteroides*, *Alistipes*, *Alloprevotella* as responders to late changes as a consequence of tumor presence (Fig. 2g). ASVs classified as *Porphyromonadaceae*, *Anaerotruncus* and *Intestinimonas* were found amongst the CRC-enriched genera correlating with high ATF6 activity in hypothesis-free TCGA dataset analyses (Extended Data Fig. 1h). We next performed a spatially resolved analysis of 16S rRNA amplicon sequencing-based bacterial profiles using individually defined 0.5 x 0.5 cm sites along the longitudinal colonic axis in fl/fl controls and tg/tg mice at the tumor (12wk) time point. In line with our previous observations [11], tumors occurred only in the proximal to mid colon (sites 1-10) and never in the distal colon (sites 11-17), with the even distribution of tumor incidence between sites indicative of equal susceptibility to tumor development (Fig. 2h). Furthermore, a reduction in the Shannon Effective diversity at all sites was observed in tg/tg mice compared to fl/fl controls (Fig. 2h). Sites in tg/tg mice were separated into three mucosal phenotypes, namely tumor (T, defined as a site containing a tumor), tumor-adjacent (TA, defined as a site directly adjacent to a T site), and non-tumor (NT, defined as a site two or more sites away from a T). The observed reduction in Shannon Effective diversity was independent of mucosal phenotype, with all three sites significantly reduced compared to the fl/fl control (Fig. 2i) Surprisingly, only NT and TA phenotypes showed significant differences in the Shannon Effective diversity within the tg/tg mucosal phenotypes (Fig. 2i). At the level of beta diversity, microbial profiles separated by mucosal phenotype (Fig. 2j). Observed shifts between genotypes rather than mucosal phenotypes, suggest ATF6 has a higher impact as a modulator of microbial community structure compared to tumor presence. In line with this, site-by-site LEfSe differential abundance analysis of the top five abundant taxa showed striking differences between fl/fl and tg/tg mice, while tumor-bearing tg/tg mice display spatial homogenization in microbial shifts along the length of the colon (Extended Data Fig. 2e). All tg/tg sites were dominated by members of *Lactobacillus*, *Mucispirillum* and *Odoribacter* (Extended Data Fig. 2e). Spatial mapping of Log_{10} transformed absolute abundance showed clear enrichment of these three early change-associated taxa, albeit mostly in both T and NT regions (Extended Data Fig. 2f). *Mucispirillum* is the only significantly enriched genus only in T regions (Extended Data Fig. 2f). To investigate the role of *Mucispirillum* in tumor development, we colonized germ-free $nATF6^{IEC}$ mice with *Mucispirillum schaedleri* at the age of 4 weeks for a 12 week period, at which tumor presence is expected. Monocolonization with *M. schaedleri* was not successful at inducing tumorigenesis, reflected in the murine survival and tumor incidence (Extended Data Fig. 3a, b). We therefore colonized mice with the synthetic Oligo-Mouse-Microbiota (OMM^{12}), consisting of 12 strains isolated from mice [31], +/- *M. schaedleri*. Despite tumor formation with an incidence of 15%, the presence of *M. schaedleri* did not impact murine survival, tumor incidence or tumor number when compared to colonization with OMM^{12} alone (Extended Data 3 a-c). Furthermore, inflammation and

dysplasia scores were similar in all colonization groups (Extended Data 3d,e), suggesting that *M. schaedleri* evidently adapts to and thrives in the altered ATF6-driven intestinal environment but is not a main contributor to tumorigenesis. To validate the suitability of the nATF6^{IEC} murine model for colonization experiments, and to investigate the potential of a human microbiota to transfer the disease phenotype, we performed fecal microbiota transplantation (FMT) of CRC patient stool into germ-free nATF6^{IEC} mice. FMT of two CRC patients (CRC1 and CRC2) significantly reduced survival in tg/tg mice (Extended Data Fig. 3f). Furthermore, CRC1 and CRC2 stool induced tumors only in tg/tg mice with an incidence of 100% and 67%, respectively (Extended Data Fig. 3g, h). Beta diversity analyses of cecal microbiota from CRC stool-associated mice showed that T and NT mice cluster separately (Extended Data Fig. 3i).

ATF6 transcriptional response alters colonic metabolism and links fatty acid biosynthesis to the presence of bacteria

To characterize the transcriptional response induced by chronic ATF6 activity and to further understand the contribution of bacteria, we performed bulk mRNA sequencing of colonic epithelial cells in fl/fl and tg/tg mice at the pre-tumor time point (5wk) under SPF and GF conditions (Fig. 3a). Transgenic chronic activation of nATF6 in SPF tg/tg mice results in a total of 1941 differentially expressed genes (DEGs; threshold: -0.5 > log2FC > 0.5, p adj. < 0.05) compared to fl/fl controls, of which 1236 DEGs are upregulated and 705 DEGs are downregulated (Fig. 3b; Supplementary Table 1, sheet 1). Functional analysis using the Kyoto Encyclopedia of Genes and Genomes (KEGG) pathways showed that almost half (16/36; blue labels) of the top and bottom ranked pathways, according to the normalized enrichment score (NES), are metabolic pathways (Fig. 3c, Supplementary Table 2, sheet 1). Under GF conditions, tg/tg mice showed a total of 706 DEGs, of which 491 DEGS are upregulated and 215 DEGs are downregulated (Extended Data Fig. 4a; Supplementary Table 1, sheet 2). Again, half of the top and bottom ranked KEGG pathways (14/28; blue labels) are metabolic pathways (Extended Data Fig. 4b, Supplementary Table 2, sheet 2). Metabolic KEGG pathways associated with SPF tg/tg mice (tumor development) and not with GF tg/tg mice (no tumor development) are amino sugar and nucleotide sugar metabolism, beta alanine metabolism, butanoate metabolism, fatty-acid (FA) metabolism, glycolysis gluconeogenesis, metabolism of xenobiotics by cytochrome P450 and nicotinate and nicotinamide metabolism. Of these, FA metabolism represents the highest ranked KEGG pathway upregulated in SPF tg/tg mice (Fig. 3c). To disentangle the transcriptional regulation between chronic tg/tg signaling under SPF and GF conditions, differentiating between the tumor-developing and non-tumor developing phenotype, we applied Signature Regulatory Clustering (SiRCle) [32]. We defined three states of genes in tg/tg mice compared to fl/fl mice for each colonization status group, namely No Change (not regulated, -0.5 < log2FC < 0.5, p adj. > 0.05), UP (upregulated,

log2FC > 0.5 and p. adj. <0.05) and DOWN (downregulated, log2FC <-0.5 and p adj. <0.05) (Fig. 3d, Supplementary Table 3, sheet 1). Following the flow of genes between SPF and GF conditions identified eight regulatory clusters named after the biological phenotype they include, for instance Core-ATF6 UP (Fig. 3 d; Supplementary Table 3, sheet 2). Depicted next to the Alluvial plot are the number and percentage of genes found in each of the clusters. After the regulatory cluster “none” (84.70%), the highest percentages of DEGs were found in the clusters “SPF-UP” (5.93 %), “SPF-DOWN” (4.27%) and “Core-ATF6 UP” (2.65%) (Fig. 3d). As anticipated, more than half (*P4hb*, *Atf6*, *Calr*, *Hspa5*, *Pdia4*, *Anxa6*, *Manf*, *Sdf2l1*, *Hsp90b1*, *Creld2*, *Nucb2*, *C1qtnf1*, *Herpud1* and *Dnajb11*) of the highly DEGs in the Core-ATF6 UP cluster (24 DEGs; black labels) are classically associated with ER protein folding and calcium homeostasis, and localized within the ER (Fig. 3e). Highly DEGs in the Core-ATF6 DOWN cluster (black labels) include *Cyba*, *Ces1g* and *Cyp4b1*, which are associated with intestinal ROS production and defense against bacteria at the colonic epithelium [33], hydrolysis of lipids and xenobiotics [34], and the hydroxylation of fatty acids and alcohols [35], respectively (Extended Data Fig. 4c). Most relevant to our murine model and the role of ATF6 signaling in colon adenoma development in tg/tg mice is the SPF UP cluster of DEGs. The highest DEG in this cluster (black label) is ER localized *Serp2*, classically involved in the UPR and protein glycosylation (Fig. 3f). Among the other highly DEGs (black labels) in this cluster, *Nup88*, *Dmxl1* and *Igf2bp3* are associated with dysplasia and cancer, including CRC [36-38]. Importantly, and in line with our findings above (Fig. 3c), the SPF UP cluster contains 23 differentially expressed FA metabolism-related genes (blue labels) (Fig. 3f; Extended Data Fig. 4d). Of note, additional analysis of the pre-tumor time point using our inducible SPF murine model (nATF6 Vil-Cre^{ERT2Tg}) addresses the transcriptional response induced by acute (4d) activation of nATF6, and demonstrates that the upregulation of the majority (13/23) of the FA metabolism-related genes (blue labels) occurs already early on after nATF6 activation (Fig. 3g, Supplementary Table 1, sheet 3). Highly DEGs in the SPF DOWN cluster (black labels) include genes that have been associated with tumor suppression and CRC [39-41] (*Meg3*, *Cwh43, Naprt)*, lipid metabolism and detoxification [42] (*Ces1f*), and bactericidal/antimicrobial activity [43] (*Iapp*) (Extended Data Fig. 4e).

Inhibition of FASN prevents tumor formation in tg/tg nATF6^{IEC} mice

Among the upregulated FA metabolism-related genes in response to both, chronic and acute activation of nATF6, FASN represents the multi-enzyme protein responsible for catalyzing FA synthesis. We stained a random subset of tissue cores from our human CRC patient cohort 1 for FASN and correlated the QuPath quantified FASN H-score with our ATF6 classification in Fig. 1a, in the same patients. Exemplary images show that patients clearly differed in their FASN expression levels (Fig. 4a). Strikingly, FASN H-scores were significantly higher in CRC

patients classified as ATF6-high compared to those classified as ATF6-low (Fig. 4b), pointing towards a positive correlation between ATF6 and FASN expression in CRC patient tissue. In a further approach, the publicly available Pan-Cancer Atlas (*n=10.967* cases including approx. 600 CRC cases) and TCGA (*n=640* CRC cases) databases were screened for genomic amplifications/gains (amp/gain) in either *ATF6* alone (*ATF6*-only), *FASN* alone (*FASN*-only) or in both genes simultaneously (*ATF6+FASN*). The relationship between *ATF6*-high and *FASN*-high patients is evident through their association classified as co-occurrence, despite not reaching significance in the TCGA database ($p=0.297$), likely due to lower case numbers compared to the Pan-Cancer Atlas database ($p<0.001$) (Extended Data Fig. 5a). While the IHC-quantified ATF6 expression did not associate with CRC patient disease–free survival in our human cohorts (Extended Data Fig. 5b-d), Kaplan-Meier analysis in both databases showed a significantly reduced disease-free survival in cases that were classed as *ATF6*-only amp/gain and those classed as combined *ATF6* and *FASN* amp/gain, compared to those cases unaltered in either of the two genes (Fig. 4c,d). Importantly, disease-free survival was significantly reduced in cases of combined *ATF6* and *FASN* amp/gain compared to those showing *ATF6*-only amp/gain in the Pan-Cancer Atlas ($p=0.0394$), with a clear trend observed in the TCGA database ($p=0.4046$) (Fig. 4c,d). Amp/gain modifications were not associated with overall survival in the two databases (Extended Data Fig. 5e,f). To understand the causal role played by FASN in colonic tumorigenesis in our nATF6^{IEC} murine model, we exposed fl/fl and tg/tg SPF mice to bi-weekly intraperitoneal injections (i.p.) of the FASN inhibitor C75 from the age of 3 weeks (pre-tumor time point) until 12 weeks (tumor time point) (Fig. 4e). Strikingly, FASN inhibition reduced tumor incidence in tg/tg mice from 80% to 0% with no tumors observed in the tg/tg colon (Fig. 4f,g). In line with this, FASN inhibition was able to reduce tumor number and tumor volume in the colon of tg/tg mice (Fig. 4h,i). Interestingly, differential abundance analysis shows that FASN inhibition leads to the depletion of *Lactobacillus* and *Odoribacter* (Fig. 4j) that were identified as dominating EC/SC taxa across all sites in the tg/tg colon (Extended Data Fig. 2e,f). Together, these findings confirm a causal role of FASN-driven microbiota shifts in tumor-susceptible tg/tg nATF6^{IEC} mice.

ATF6-enriched LCFAs drive dysbiotic microbiota adaptation

ATF6 signaling clearly alters epithelial metabolism and the intestinal microbiota. To understand its effects on the metabolome, we performed untargeted metabolomics of cecal content at pre-tumor (5wk), tumor (12wk) and late-tumor (20wk) time points using LC-TOF-MS. Principal component analysis revealed a drastic difference in the metabolome between tumor-bearing mice (red) and non-tumor mice (blue), while metabolite profiles clustered in closer proximity for all three genotypes at the pre-tumor time point (Extended Data Fig. 6a). Differential enrichment analysis at the tumor time point demonstrated a depletion of peptide metabolites

and sphingolipids, while long-chain fatty acids (LCFA) and other complex lipid species were enriched in tg/tg mice (Extended Data Fig. 6b). Principal component analysis showed that lipid profiles of non-tumor (NT) mice separate from tumor (T) mice already at the pre-tumor time point, with increasing diversity over time (Extended Data Fig. 6c). Differential metabolite analysis of the significantly regulated metabolites, shown between all genotypes and time points, demonstrated that tg/tg associated metabolites are mostly comprised of lysophospholipids and LCFAs (Extended Data Fig. 6d). Multi-omic data integration based on the mixOmics R Package using sPLS-DA analysis identified a distinct cluster of tumor-enriched metabolites and ASVs (Extended Data Fig. 6e). By sorting correlated ASVs and metabolites using feature importance, we identified *Lactobacillus* as well as LCFAs and lysophospholipids as microbial and metabolite contributions, respectively (Extended Data Fig. 6f). To understand whether LCFA enrichment was tumor- or ATF6-driven, we examined the identified microbiota-correlated LCFAs from the integration analysis at all three time points. An unknown C20 hydroxy fatty acid and nervonic acid (FA 24:1) were the only LCFAs enriched in tg/tg mice at the pre-tumor time point, with higher significance reached across all LCFAs at the tumor and late-tumor time points (Fig. 5a), showing that tumor presence increases the LCFA pool. Next, to assess whether the identified LCFAs modify the microbial community structure of our identified pre-tumor changed bacteria (Fig. 2g), we computed correlation networks between each of the microbiota-covariant fatty acids, clr-transformed abundance of EC/SC-related ASVs, as well as community metrics (alpha and beta diversity). The majority of taxa were positively correlated with at least one LCFA at the 5wk time point, however a cluster of highly positively correlated ASVs and metabolites was observed comprising an unknown C20 hydroxy fatty acid, docosapentanoic acid (FA 22:5), nervonic acid (FA 24:1) and fatty acid ester of hydroxy fatty acid (FAHFA 22:6/3:0), along with ASVs classified as *Lactobacillus* and to a lesser extent *Mucispirillum* (Fig. 5b). Interestingly, docosahexanoic acid (FA 22:6) correlated negatively with several alpha diversity metrics (Richness and Shannon Effective) as well as positively with GUniFrac dissimilarity (Fig. 5b), suggesting this LCFA may alter community structure to allow colonization of EC or SC taxa. In line with this, *Mucispirillum* was positively correlated with docosahexanoic acid (FA 22:6) (Fig. 5b). Surprisingly, *Odoribacter* showed mostly negative correlations (Fig. 5b).

To further characterize the altered lipid environment in tg/tg mice, we quantified total FAs in colonic tissue using GC-MS. Analyses revealed an increase in saturated fatty acids (SAFAs) in T compared to NT mice, which also correlated with tumor number (Fig. 5c,d). Furthermore, T mice show a clear elongation of SAFAs including FA 20:0 and FA 22:0 compared to NT mice (Fig. 5e). To determine whether elongation is a direct consequence of ATF6 signaling, we assessed ATF6-mediated elongation of FAs in *ex vivo* colonic organoid cultures. We first phenotypically characterized colon organoids derived from fl/fl controls and tg/tg mice at the

late-tumor time point (20wk). Both fl/fl and tg/tg crypts formed viable organoids in culture, including cyst formation (d1) and budding (d7) of cysts (Fig. 5f). Strikingly, tg/tg organoids in culture did not show any significant increase in organoid size (Fig. 5g) or the number of budding crypts per cyst (Fig. 5h) compared to fl/fl controls, indicating that the hyper-proliferative phenotype observed *in vivo* in the presence of the microbiota is lost in this *ex vivo* culture system. In a separate experiment, intestinal organoids from nATF6 Vil-Cre^{ERT2} (fl/fl^{ERT2} and tg/tg^{ERT2}) mice were cultured, and *ATF6* expression induced by adding 500nM (Z)-4-hydroxytamoxifen (4-OHT) to the culture medium for 24h. This was followed by a 24h exposure of organoids to deuterated eicoseinoic acid (D_3-FA 20:0) (Fig. 5i). Importantly, tg/tg^{ERT2} intestinal organoids showed a significantly increased potential of FA elongation, quantified as the percentage of metabolized D_3-FA20:0 to D_3-FA:22:0, compared to fl/fl^{ERT2} controls (Fig. 5j). The above findings demonstrate that ATF6 activation is the driver of FA elongation in the absence of microbial and immune signaling.

LCFA compounds are known to be toxic to bacteria, requiring adaptation mechanisms to allow growth in FA-rich milieus. Using PICRUSt2, we generated predictions of genomic content [44,45]. A strong enrichment of FA metabolism pathways (labeled blue) was observed between the pre-tumor (5wk) and tumor (12wk) time points, with a weak enrichment observed between NT and T samples (Extended Data Fig. 7a). Furthermore, we identified genes involved in bacterial responses to FAs in the proximal tumor-susceptible region of the colon, which are known to be involved in FA detoxification, catabolism and efflux (Extended Data Fig. 7b). Of this FA-response signature, oleate hydratase (*ohyA*) and the FA efflux pump (*farE*) was observed to be upregulation in tumor mice compared to controls (Extended Data Fig. 7b). *OhyA* mediated fatty acid hydroxylation enables growth of certain bacteria in lipid-rich environments [46]. Spatial mapping of $\log_{10}$ transformed relative abundance showed clear enrichment of *ohyA* across all sites in tg/tg mice compared to fl/fl controls (Fig. 5k). The relative abundance of *ohyA* was increased in tumor-bearing tg/tg mice compared to fl/fl controls (Fig. 5l). Furthermore, the ratio of *ohyA*+ to *ohyA*- taxa was increased in all three mucosal phenotypes in tg/tg mice, compared to fl/fl controls (Fig. 5m). *FarE* constitutes a lipid efflux pump associated with antimicrobial FA resistance to limit the cellular accumulation of toxic FAs [47]. Similar to *ohyA*, we observed an increased relative abundance across all tg/tg sites (Fig. 5n), and increased relative abundance of *farE* in tumor-bearing tg/tg mice (Fig. 5o). Furthermore, the ratio of *farE*+ to *farE*- taxa was increased in all tg/tg mucosal phenotypes, compared to fl/fl controls (Fig. 5p). We next assessed the taxonomic contributions associated with predicted functional shifts in *ohyA* and *farE* abundance in tg/tg mice. *Lactobacillus* and an unknown Lachnospiraceae accounted for the largest share of *ohyA* abundance across all three mucosal phenotypes, making up 19.4-34.2% and 32.2-49.6%, respectively (Extended Data Fig. 7c). In case of *farE*, *Lactobacillus* almost exclusively accounts for *farE* abundance, making up 99.9% across all three mucosal

phenotypes in tg/tg mice (Extended Data Fig. 7d). We had previously identified *Lactobacillus* to be associated with the SC and LC group, and Lachnospiraceae with the EC group (Fig. 2g). Taken together, our findings clearly indicate an early pre-tumor microbial adaptation to the ATF6-altered FA-rich intestinal environment, to shape a tumor-associated bacterial lipid-response signature.

Discussion

As the second leading cause of deaths worldwide [48], early and accurate diagnosis as well as novel treatment strategies are imperative in the management of CRC. As a fundamental mediator in the pathogenesis of CRC, the UPR^{ER} represents a promising host cellular mechanism for preventive and therapeutic intervention. While our mechanistic understanding of the role of ATF6 signaling in CRC remains limited, its involvement in tumor growth, metastasis and relapse has been observed [13-15]. In the present study, we demonstrate the relevance of ATF6 expression in CRC patients across multiple independent German CRC cohorts by identifying a clear sub-population (19-38%) of patients that present with high ATF6 expression, underlining the importance of ATF6 in CRC. Most importantly, we identified a mechanism through which ATF6-mediated changes in cellular lipid metabolism of the intestinal epithelium contribute to the development of tumor-promoting microbiota changes at an early disease stage.

We previously showed that the chronic activation of nATF6 specifically in murine intestinal epithelial cells ($nATF6^{IEC}$) results in microbiota-dependent early-onset colonic adenomas [11]. The necessity of microbial triggers in tumor induction was shown via germ-free (GF) mice, which remained tumor-free [11]. Furthermore, the transfer of pre-tumor murine cecal content into GF mice revealed the dysbiotic microbiota from tumor-susceptible mice to have an increased capacity to induce tumors [11]. Importantly, dysbiosis in $nATF6^{IEC}$ mice precedes tumorigenesis [11], suggesting that tumor-independent mechanisms at early stages of the ATF6-driven pathogenesis initiate microbial changes. To ascertain these mechanisms, we set out to characterize the transcriptional response induced by chronic ATF6 activation in the presence (SPF) and absence (GF) of bacteria at the pre-tumor stage. We identify the FA metabolism KEGG pathway as one of the top ranked metabolic pathways altered in tumor-susceptible SPF mice, and detect 23 upregulated FA metabolism-related genes. The majority are upregulated already in response to acute ATF6 activation, confirming FA alterations to be an early event occurring in direct response to ATF6 signaling in the presence of the microbiota. Lipid metabolic rewiring forms a phenotypic hallmark of cancer, with altered lipidome profiles identified in tumors of numerous organs, including the colon [18,20,24,49]. While the specific contribution of ATF6 to lipid metabolism is less well understood, the UPR^{ER} is known to play an important role in lipid metabolism [50-53]. Ecker *et al.* recently identified a robust tumor-specific triglyceride species signature that correlates with postoperative disease-free survival in a multicohort study spanning two clinical centres [24]. Moreover, *FASN* gene expression was prognostically detrimental [24]. Strikingly, the *in vivo* inhibition of the multi-enzyme complex FASN in $nATF6^{IEC}$ mice, responsible for catalyzing FA synthesis, results in the prevention of colon adenoma development. We show that our tumor-associated cecal metabolite signature

is mostly comprised of lysophospholipids and LCFAs, with further analyses of colonic tissue displaying increases in SAFAs and LCFAs. These findings are in line with a study profiling FAs in tissue and plasma of CRC patients and healthy controls, which identified a CRC-associated FA panel and found that very long chain FAs (VLCFAs) were the most increased FAs [54]. Our experimental approach in *ex vivo* organoids demonstrates that FA elongation is a direct consequence of ATF6 signaling, occurring in the absence of microbial signals.

In addition to CRC-associated lipid signatures, CRC-associated microbial signatures have also been identified [55,56]. In a hypothesis-free approach analyzing transcription factor activity and microbial profiles in CRC patients we show *ATF6* activity to positively associate with the presence of such a risk profile associated bacterial genera, identifying a clear link between ATF6 signaling and the microbiota in CRC pathogenesis. In a comprehensive spatially- and time-resolved 16S rRNA sequencing analysis of the mucosa-associated microbiota of SPF nATF6^{IEC} mice, we identify bacteria that are associated with early, sustained and late stages in ATF6-driven tumorigenesis. Of note, the human CRC-enriched genera overlap with ASVs classified as *Porphyromonadaceae*, *Anaerotruncus* and *Intestinimonas* in the murine model. Spatially, all tumor mice are dominated by three EC/SC-associated genera, namely *Lactobacillus*, *Mucispirillum* and *Odoribacter*. Interestingly, we observe that tumor prevention following FASN inhibition is associated with a depletion in *Lactobacillus* and *Odoribacter,* pointing towards a causal role of FASN-driven microbiota shifts in ATF6-driven tumorigenesis. A handful of studies have identified pro-oncogenic bacteria enriched in adenoma samples, however, questions remain over whether these taxa initiate disease, since adenoma formation induces metabolic alterations that likely impact the local microenvironment and alter microbial composition [57-59]. Our knowledge on which triggers may enable taxa to expand early on, and potentially become tumor-promoting, is sparse. We hypothesize that ATF6-driven lipid alterations impact the intestinal microbiota as an early event of tumorigenesis in nATF6^{IEC} mice. Our Multi-omic data integration of cecal metabolites with mucosal microbiota profiles identifies microbiota-correlated increases in LCFAs already at the pre-tumor time point, suggesting a clear link between ATF6-induced lipid alterations and changes in the intestinal microbiota preceding tumorigenesis. Importantly, and in support of our hypothesis, PICRUSt2 predictions of genomic content confirm that the ATF6-driven FA-rich intestinal environment results in microbial adaptation and a lipid-response signature associated with genes involved in FA detoxification, catabolism and efflux. Increased relative abundances were accounted for by *Lactobacillus* and an unknown Lachnospiraceae, both of which were associated with tumor-susceptible mice in our longitudinal bacterial classification approach.

In conclusion, we identify a clear mechanistic sequence of events in the initiation of colon tumorigenesis whereby ATF6 signaling drives a clinically relevant pathologic response by altering lipid metabolism to induce microbial adaptation, ultimately leading to a tumor-relevant

bacterial dysbiosis. Although beyond the scope of this study, future work should focus on single-cell transcriptomics to characterize the ATF6 transcriptional response at the cellular level, as well as extending gnotobiotic mouse experiments with individual bacterial candidates, to identify causal tumor drivers and elucidate mechanisms of tumor initiation. Together, the above highlight novel mechanistic findings in an exciting new avenue of research bringing together cellular stress responses, lipid metabolism and the intestinal microbiota in the context of CRC. This evident triangular interplay presents new targetable vulnerabilities in CRC that warrant future research efforts to identify potential future prevention and treatment strategies.

Funding

This work was funded by the Deutsche Forschungsgemeinschaft (DFG, German Research Foundation) Collaborative Research Center CRC1335 (Aberrant immune signals in cancer; project no. 360372040; P11) and CRC 1371 (Microbiome signatures: functional relevance in the digestive tract; project no. 395357507; P13 and P18), as well as the Bundesministerium für Bildung und Forschung (BMBF, Microbiome-based Prevention of Early-Onset Colon and Rectal Cancer (Mi-EOCRC); project no. 100509410).

Competing interests: None

The authors declare no competing interests.

Author contributions

OC and DH wrote the manuscript. OC, AS, SB, JK, MS and DH designed the experiments and performed data analysis. AS, JK and MS performed mouse experiments and respective mouse tissue and microbiota processing and analysis. BS provided the OMM[12] consortium. KS performed IHC staining on human cohort TMAs. OC performed the quantification and data analysis of human IHC staining. TM supported quantification of human IHC staining. MJ provided CRC cohort 1 tissue and supported data analysis. KPJ provided CRC cohort 2 tissue and generated TCGA survival curves. CS, SH, CR (Christoph Röcken) and CR (Christian Röder) provided CRC cohort 3 tissue and supported data analysis. DMC, SW and TP performed ATF6 quantification validation classification and regression models. JW and GZ performed microbial and transcription factor TCGA analyses. SB prepared mouse tissue for mRNA sequencing samples and supported mRNA sequencing analyses. PR performed mRNA sequencing. CS and TK performed mRNA sequencing data analyses. AD performed untargeted metabolomics. JP (Josh Pauling) and NK performed metabolomics analysis and integration. JP (Johannes Plagge), JE and GL performed fatty acid analyses and data analysis.

ORCID IDs

Olivia Coleman https://orcid.org/0000-0002-4075-7820

Adam Sorbie https://orcid.org/0000-0002-3330-4612

Nikolai Köhler https://orcid.org/0000-0002-5103-883X

Jakob Wirbel https://orcid.org/0000-0002-4073-3562

Christina Schmidt https://orcid.org/0000-0002-3867-0881
Tim Kacprowski https://orcid.org/0000-0002-5393-2413
Andreas Dunkel https://orcid.org/0000-0002-4445-6144
Johannes Plagge https://orcid.org/0000-0002-7180-8221
Tingying Peng https://orcid.org/0000-0002-7881-1749
Thomas Metzler https://orcid.org/0000-0002-1620-5559
Bärbel Stecher https://orcid.org/0000-0002-7445-5193
Philipp Rosenstiel https://orcid.org/0000-0002-9692-8828
Katja Steiger https://orcid.org/0000-0002-7269-5433
Moritz Jesinghaus https://orcid.org/0000-0002-0018-5661
Gerhard Liebisch https://orcid.org/0000-0003-4886-0811
Georg Zeller https://orcid.org/0000-0003-1429-7485
Klaus-Peter Janssen https://orcid.org/0000-0002-4707-7887
Dirk Haller http://orcid.org/0000-0002-6977-4085

Online Methods

Ethics statement regarding animal experiments. All animal experiments, as well as maintenance and breeding of mouse lines, were approved by the Committee on Animal Health Care and Use of the state of Upper Bavaria (Regierung von Oberbayern; AZ ROB-55.2-1-54-2532-217-2014, AZ ROB-55.2-2532.Vet_02-20-58, AZ TVA 55.2-2532.Vet_02-18-149, AZ TVA 55.2-2532.Vet_02-18-121, AZ TVA 55.2-2532.Vet_02-19-006) and performed in strict compliance with the EEC recommendations for the care and use of laboratory animals (European Communities Council Directive of November 24, 1986 (86/609/EEC)).

Ethics statement regarding patient samples. Immunohistochemistry staining and quantification of ATF6 were performed in three independent human cohorts: a German large single-center cohort comprising 1004 colorectal cancer patients that underwent surgical resection spanning two decades, for which 959 patient tissue samples could be quantified (cohort 1) [28], a German cohort consisting of 104 CRC patients followed up over 20 years, for which 50 patient samples could be quantified (cohort 2), and a German single center cohort comprising more than 1,500 resected CRC patient samples spanning approximately 25 years, for which 55 EOCRC (age <50y) and 256 LOCRC (age >50y) were obtained and could be quantified (cohort 3). The use of surgically resected human tissue samples was approved by the local Ethics Committee of the Technical University of Munich (TUM) (ref.-no. 252/16 s, cohort 1), by the Ethics Committee of the Medical Faculty of TUM (ref.-no. 1926/7, 375/16S and 2022-169-S-KH, cohort 2), and by the local Ethics Committee of the University Hospital Schleswig-Holstein (ref.-no. A 110/99, cohort 3). CRC patient cohort 3 tissue specimens were supplied by the biobank TRIBanK (Translational Interdisciplinary Biobank Kiel) together with the Institute of Pathology, University Hospital Schleswig-Holstein, Kiel, Germany. Patient samples from all three cohorts were obtained after prior informed written consent.

Immunohistochemical staining and quantification of ATF6. TMA cores were immunohistochemically stained with an anti-ATF6 antibody (Sigma-Aldrich, HPA-005935) diluted 1:100, following antigen retrieval in an EDTA buffer (30 min, pH 9), or an anti-FASN antibody (LS Bio, LS-B3636) diluted 1:200 following antigen retrieval in a Citrate buffer (20 min, pH 6). Nuclei were counterstained with hematoxylin (Waldeck). Stainings were performed using the Leica Bond RXm (Leica) and scanned using the Aperio AT2 (Leica Biosystems). ATF6- and FASN-stained TMA cores were quantified using the QuPath Software [29]. Cells were identified through positive cell detection of the hematoxylin-positive nucleus. ATF6 staining intensities for the nuclear and the cytoplasmic regions were classified according to defined thresholds of the DAB OD max and DAB OD mean, respectively. FASN staining was quantified based on cytoplasmic regions only. Furthermore, the object classifier was trained and applied to distinguish between epithelial cells and stromal cells. Exported epithelial histochemical-

scores (H-scores, capturing both the intensity and the percentage of stained cells) for the nucleus and the cytoplasm were used for further patient cohort analyses. The H-score cut-off was determined using the online *Cutoff Finder* Web Application for Biomarker cutoff optimization [60].

ATF6 expression analysis using AI. Whole slide images were segmented using QuPath into individual cores and scaled down to 312x312 pixels. This pre-processing step yielded a dataset of 176 TMA cores from a cohort of 50 patients (cohort 2). For our deep learning model, a ResNet18 was trained (arXiv:1512.03385v1 [cs.CV]), freezing all layers except the final convolutional and fully connected layers for the classification task and freezing the first layer for the regression task. This allowed leveraging pre-trained features while fine-tuning the model's output layers for our specific task. To improve model generalization, data augmentation techniques were applied, including random horizontal and vertical flips and random rotations. In the final layer, dropout regularization was incorporated to prevent overfitting. A 5-fold cross-validation was conducted to evaluate our model's performance. Each fold used data from 40 patients for training and 10 patients for validation. Throughout cross-validation, the best models were recorded based on their accuracy (classification task) or loss (regression task) in the validation dataset. Their weights were preserved for subsequent use. In our final prediction task of classifying samples as ATF6-high or ATF6-low, a weighted average ensemble strategy was employed by combining the predictions of the five best models. In a final validation step, our ensemble's predictions were tested on an entirely independent cohort comprising 918 patients (cohort 1).

TCGA Dataset. For both CRC-related TCGA projects (TCGA-COAD and TCGA-READ), gene expression profiles were downloaded from the firebrowse.org website (RSEM normalized gene expression). Using those tables, transcription factor activities were inferred using the DoRothEA R package (version 1.10.0) [61] with default parameters (using transcription factor-target interactions of medium- or higher confidence (A-C) and using the viper algorithm for statistical inference). Bacterial profiles derived from whole exome sequencing of the same samples were extracted from the supplemental material of Dohlman *et al.* [30]. For all samples present in both data types (610 samples overlap: 451 COAD, 159 READ), the inferred activity of ATF6 was associated with bacterial presence, using the project information as random effect in a random effect model implemented in the lmerTest R package [62]. Since we observed microsatellite instability (MSI) status to be very strongly associated with both bacterial profiles and ATF6 activity, we additionally included MSI-status as another random effect in a second association model. Bacterial genera were tested for CRC-enrichment with a random effects model for all patients with paired tumor and normal tissue samples and significantly CRC-

enriched genera are highlighted in Figure 1 and Extended Data 1. All *p*-values were corrected for multiple hypothesis testing using the Benjamini-Hochberg procedure [63].

Sampling of murine cecal content and colonic mucosa-associated microbiota. Cecal content was harvested immediately after euthanization and stored at -80°C before DNA extraction. The murine colon was excised and opened longitudinally before clearing of colonic content using a sterile needle and sterile PBS washes. Tissue sections were then excised using a sterile scalpel pre-treated with DNA Away™ (Fisher Scientific) to destroy contaminating DNA fragments. For spatial microbiota analyses, the entire colon was laid on a grid and dissected into individual 0.5 cm x 0.5 cm sections and subsequently frozen at -80°C before DNA extraction. All steps were carried out in a laminar flow cabinet.

Microbial DNA extraction from murine cecal content and colonic tissue. DNA extraction from frozen cecal content was carried out using a modified version of the protocol described by Godon et al [64]. Briefly, cecal samples were homogenized by vortexing and transferred to autoclaved screw-cap Eppendorf tubes containing 500mg silica beads (0.1mm Carl Roth) and kept on ice. To this, 600µl of DNA stabilizer (Macherey Nagel), 250µl 4M Guanidine thiocyanate and 500µl 5% N-laurolyl-sarcosine was added. Samples were incubated under moderate shaking (700rpm) for 1 hour at 70°C. Lysis was achieved via mechanical disruption with a FastPrep ®-24 bead beater (MP Biomedicals) using three 40-second cycles at a speed of 6.5 m/s. 15mg Polyvinylpolypyrrolidone (PVPP; Sigma-Aldrich) was added to homogenate to remove phenol contamination, before centrifugation at 15,000×g for 3 minutes at 4°C. The resulting supernatant was recovered, and centrifuged again under the same conditions, resulting in a clear supernatant containing lysed bacterial cells. To this mixture, 10mg/ml RNase was added to degrade bacterial RNA and incubated at 37°C for 30 minutes under constant shaking (700rpm). DNA extraction from colonic tissue was performed using enzymatic digestion. Where possible samples were extracted using the same kit batch, to limit differences in inherent kit contamination between different batches [65]. Tissues were placed in 180µl sterile lysis buffer (20Mm Tris/HCL, 2Mm EDTA, 1% Triton-X100; pH 8 supplemented with 20mg/ml lysozyme) and incubated for 1 hour in a shaking incubator (950rpm) at 37°C. 10mg/ml Proteinase K (Macherey Nagel) was then added, and samples were incubated for 1-3 hours (until complete lysis of the tissue was obtained) at 56°C under moderate shaking (950rpm). The resulting genomic DNA was then purified using the NucleoSpin® gDNA clean-up kit (Macherey Nagel), according to the manufacturer's instructions. The concentration and purity of extracted genomic DNA was determined using a Nanodrop ND-1000 Spectrophotometer. Samples were stored at -20°C before sequencing. In order to quantitatively determine the number of 16S rRNA gene copies in a given sample a known amount of artificially constructed 16S rRNA sequences were added. Spiked samples were

processed as above, except mucosal samples were weighed before and after the addition of lysis buffer to which 1µl solution containing artificially constructed 16S rRNA sequences at a concentration of 150pg/ml prior to extraction. Spike-in sequences were adapted from Tourlousse *et al.* and are listed in Supplementary Table 4 [66].

16S rRNA gene amplicon sequencing. High throughput amplicon sequencing of the 16S rRNA gene was carried out as previously described [67]. In brief, the V3 and V4 hypervariable regions were amplified via a 2-step protocol, using the 341f and 785r primer pair (341f 5'-CCTACGGGNGGCWGCAG-3', 785r 5'-GACTACHVGGGTATCTAATCC-3'). With 10x15 cycles for cecal content samples and 15x15 for mucosal samples. Samples were barcoded with a double index, according to Kozich *et al.* [68]. The resulting amplicons were purified using AGENCOURT AMPure XP Beads (Beckman Coulter, Krefeld, Germany), pooled in equimolar ratios and then sequenced on an Illumina MiSeq system (Illumina), in paired-end mode (2 x 275bp). Raw reads were processed using IMNGS, which wraps the UPARSE/USEARCH software pipeline [69,70]. Sequences were demultiplexed, trimmed to first base with a quality score <3 and merged. To remove spurious sequences, a length filter was applied based on the expected amplicon size of 444bp, removing those smaller than 300 and larger than 600bp. The resulting paired sequences were then dereplicated and denoised using UNOISE3, to generate Amplicon sequence variants (ASVs; also known as zero-radius OTUs or zOTUs), reflecting true biological sequences [71]. Artificial 16S rRNA sequences in spiked samples were first enumerated and then removed using a custom python script, running BLAST to align ASV reference sequences against the spike sequences [72]. Taxonomy was assigned using the RDP classifier version 2.11 [73]. Samples with less than 5000 total reads were excluded from further analysis. Since low biomass samples are susceptible to contamination which can lead to spurious conclusions, all mucosal samples were further processed with the R package decontam to remove putative contaminants [74]. This package utilises the relationship between pooled DNA concentration prior to sequencing and the prevalence and abundance of taxa in negative controls to identify putative contaminants. Identification of contaminants was performed with the isContaminant function using default parameters.

Downstream analyses were performed using Rhea and phyloseq [75,76]. Briefly, ASV tables were normalized using minimum sum scaling or relative abundance. Alpha diversity was measured using Richness, Shannon Effective and for phylogenetic diversity, Faith's phylogenetic diversity (Faith's PD) [77]. To assess differences between groups, beta diversity was calculated based on generalized UniFrac distance (GUniFrac) [78]. Mean GUniFrac dissimilarity for a given sample was calculated as the dissimilarity to the respective control mean. Differentially abundant taxa were identified using the Linear Discriminant analysis Effect size (LEfSe)

algorithm, with a Linear discriminant analysis threshold (LDA) threshold of 3.0, to limit false positives [79,80].

The total 16S copy number based on spike-in measurement was calculated using the formula:

$$Absolute\ abundance = \frac{\left(\frac{s}{r}\right) * n}{\left(\frac{b}{w}\right)}$$

where *s* is the spike-in reads per sample, *r,* a randomly chosen sample to adjust to, *n* spike DNA concentration in ng, *b* bacterial reads per sample and *w,* the weight of the respective sample.

Supervised classification of 16S rRNA sequencing. Supervised classification of mucosal and luminal microbial profiles in non-tumor (fl/fl and tg/wt) and T (tg/tg) mice was performed using the SIAMCAT R package, utilising Ridge-regression (RR), LASSO regression (L1L) and Random forest (RF) models, which were chosen based on the ease of interpretation of model output [81,82]. To account for differences in sample size between mucosal and luminal data, mucosal data was randomly subsampled to match luminal data. Prior to model training, low prevalent features - defined as those present in less than one-third of samples - were removed, and the data transformed using a centred log-ratio transform. Feature selection was performed using an area under the curve (AUC) threshold of 0.75 and nested within the cross-validation (CV) procedure to avoid artificial inflation of model AUC. All models were trained using five-fold CV, or in case of smaller sample size (<50 total samples), leave-one-out CV (LOOCV), each with five rounds of resampling.

Colonization of germ-free mice with OMM12+/- *M. schaedleri*. *M. schaedleri* was kindly provided by Bärbel Stecher (German center for infection research, LMU, München, Germany) and cultured as previously described [83]. Briefly, *M. schaedleri* was grown in Akkermansia medium (AAM) + 10mM $NaNO_3$ medium in Hungate tubes for 48h under anaerobic conditions and overpressure. The cultured bacterium was aliquoted, mixed 1:1 with 20% glycerol (v/v) (Fisher), and stored at -80°C until used. For the preparation of Oligo-MM[12] gavage, all bacterial strains were grown individually in Hungate tubes with AAM medium (previously gassed with N_2) for 24-48h under anaerobic conditions. In order to mix the bacteria in the same amount, bacterial growth was measured with a photometer (OD600) and adjusted accordingly. The bacterial mix was then aliquoted, mixed 1:1 with 20% (v/v) glycerol and stored at -80°C until used. Germfree mice were gavaged at the age of four weeks and colonized for 12 weeks. Mice were gavaged twice orally and rectal on day 0 and day 3. All mice were euthanized with CO_2 at the end of an experiment or when abortion criteria were met.

Colonization of germ-free mice with CRC patient stool. Stool samples obtained from CRC patients were collected and immediately mixed 1:1 with 20% glycerol (v/v) (Fisher), and stored at -80°C until use. For the preparation of gavage, stool samples were thawed, homogenized by vortexing and aliquoted to avoid thaw-freeze cycles. On the day of the gavage, one aliquot was thawed, centrifuged at 4°C at 300xg for 3 minutes to remove residuals. The supernatant was then centrifuged at 4°C at 8000xg for 10 minutes to pellet the bacteria. The pellet was solved in sterile PBS and transferred into a sterile hungate. Germ-free mice were gavaged once orally at the age of four weeks and colonized for 12 weeks. All mice were euthanized with CO_2 at the end of an experiment or when abortion criteria were met.

Isolation of primary colonic IECs. Colonic tissue was longitudinally opened, and transferred to 20 mL Dulbecco's modified Eagle medium (Gibco) containing 10% fetal calf serum, 1% L-glutamine, and 0.8% antibiotics/antimycotics (IEC isolation medium) supplemented with 1 mmol/L dithiothreitol (Roth). The tissue was vigorously vortexed for 1 minute, incubated under continuous shaking (37°C, 15 minutes) and vortexed again for 1 minute. The cell suspension was centrifuged (7 minutes, 300xge) and the cell pellet was resuspended in 5 mL IEC isolation medium. After vortexing for 1 minute, the remaining tissue pieces were incubated in 20 mL PBS (10 minutes, 37°C) containing 1.5 mM EDTA under continuous shaking. The cell suspension was vortexed again followed by another centrifugation to pellet the cells. Both cell suspension fractions were combined and purified by centrifugation through a 20%/40% (in medium/PBS) discontinuous Percoll gradient (GE Healthcare Life Sciences) at 600xg for 30 minutes. The IEC cells at the interface between the two Percoll phases were collected and washed twice (with medium/PBS). The isolated IECs were lysed in RA1 RNA lysis buffer (Macherey-Nagel).

RNA Isolation and library construction. RNA of colonic IECs was isolated according to the manufacturer's instructions (NucleoSpin RNAII kit, Macherey-Nagel) and measured by NanoDrop ND-1000 spectrophotometer (Thermo Fisher Scientific). TruSeq stranded Total RNA kit (Illumina) was used for the construction of strand-specific sequencing libraries from the isolated colonic IEC RNA. Sequencing was performed on an Illumina HiSeq2500 (75-nucleotide (nt) paired-end reads for each run, 1/10 lanes per sample.

RNASeq preprocessing. After the initial trimming of reads using trim_galore (version 0.6.4) to satisfy a Phred score of at least 30, RNASeq data was processed with the 'nf-core/rnaseq' pipeline (version 1.4.2) and aligned to the GRCm38 genome using the 'STAR' aligner (version 2.6.1d). Quantification of transcripts was performed using Salmon (version 0.14.1). All sequence properties were inspected in MultiQC and passed the quality thresholds. Raw and processed RNASeq data will be uploaded to GEO.

RNAseq functional analysis. Gene Set enrichment analysis (GSEA) was performed using the differential expression results ranked by t-value [84]. KEGG gene set was downloaded from the Molecular Signatures Database [84-86]. Gene names were translated into mouse gene names before the analysis using scibiomart (v.), a wrapper around the API from BioMart. GSEA was performed using the packages fgsea [87] (v1.24.0) and GSEABase [88] (v 1.60.0). Next we performed regulatory clustering based on regulatory rules (Supplementary Table 3, sheet 2) using sircleR package function sircleRCM_2Cond [32]. In brief, each gene was assigned to "UP" (log2FC > 0.5, *p*.adj <0.05), "DOWN" (log2FC < -0.5, *p*.adj <0.05) or "No Change" (0.5 > log2FC > -0.5 and/or *p*.adj > 0.05) based on its expression change between fl/fl versus tg/tg. The background method chosen was "C1&C2", which means a gene had to be detected in both conditions in order to be included in the clustering. Plots were generated using the EnhancedVolcano package [89] (v1.16.0) and ggplot2 [90] (v 3.4.2).

Intraperitoneal injections of mice with FASN inhibitor C75. The FASN inhibitor C75 (Biomol) was dissolved in RPMI 1640 (Sigma Aldrich) to a final concentration of 1.5 mg/mL, aliquoted and stored at -20°C until used. C75 or RPMI were injected intraperitoneally (i.p.; 10 ml/kg body weight) biweekly, starting at the age of three weeks until twelve weeks of age (tumor time point). When necessary, mice were given a subcutaneous depot (1:1 mixture (v/v) of 5% glucose and ringer's lactate (B. Braun)) to alleviate potential side-effects of C75. Mice were euthanized with CO_2 at the age of twelve weeks or when abortion criteria were met.

Untargeted metabolomics of murine cecal content or tissue. Sample preparation was performed as previously described [67]. Briefly, mouse cecal content (~20mg) or tissue (~25mg) was mixed with 1ml methanol-based extraction solvent in a 2ml bead beater tube (CKMix 2ml, Bertin Technologies) filled with ceramic beads (1.4 mm and 2.8 mm ceramic beads). Samples were then homogenized using a bead beater (Precellys Evolution, Bertin Technologies) supplied with a Cryolys cooling module (Bertin Technologies, cooled with liquid nitrogen) three times for a duration of 20 seconds, at a speed of 8000rpm. Subsequently, the resulting suspension was centrifuged for 10 minutes, at 6000rpm. Finally, 100µl of supernatant was mixed with 20µl internal standard solution (7 µmol/l) and injected into the Liquid chromatography time-of-flight mass spectrometer (LC-TOF-MS) system for untargeted analysis. Untargeted LC-TOF-MS analysis was carried out as described in Metwaly *et al.* [67]. Briefly, untargeted analysis was performed on an ExionLC Ultra-high performance liquid chromatography (UHPLC) system (Sciex), connected to a 6600 TripleTOF instrument (Sciex) operating in positive and negative electrospray mode and calibrated using ESI positive and negative calibration solutions (Sciex). UHPLC phase separation was performed in reverse as well as hydrophilic interaction stationary phase (HILIC), on a Kinetex C18 column (Phenomenex) and ACQUITY BEH Amide column (Water) respectively. Mass spectrometry

was performed using SWATH mode, with fragment spectra recorded in high-sensitivity mode. Metabolomics data processing was performed as described previously [67]. Briefly, Raw data files were converted into Reifycs Abf (Analysis Base File) files and subsequent untargeted peak picking was performed using MS-DIAL software (version 3.5274) [91]. Alignment was performed across all samples and the peak area of individual features were exported for further analysis using the R statistical software environment. Peak normalisation was based on QC samples, employing the method described in Wehrens *et al.* [92]. All features were then combined into a single table and further normalised according to sample weight, before analysis.

Multi-omics integration. Integration of metabolomic and microbiota data was performed on log-transformed, scaled, and centred log-ratio (clr) transformed metabolite and ASV matrices, respectively. General associations between the microbiota and metabolites were identified using a multi-block sparse partial least squares discriminant analysis (sPLS-DA) model with seven components and 10-fold CV, as implemented in the DIABLO framework of the mixOmics R package [93,94]. Associations between ASVs and metabolites were determined using Spearman's rank correlation, using the corrr R package [95].

Functional potential prediction. To calculate predicted functional profiles based on 16S rRNA sequencing data, we utilised PICRUSt2 version 2.3 [44]. FASTA files of representative sequences and minimum sum scaled ASV tables were used as input for the command: *picrust2_pipeline.py*, which runs the full PICRUSt2 pipeline, aligning and placing the sequences into a reference tree, calculation of 16S copy number, Enzyme Commission (EC) and KEGG orthologs abundances, adjustment of these by 16S abundance and finally infers MetaCyc pathways by collapsing EC numbers according to their associated metabolic pathway. All PICRUSt2 data were generated in a high-performance computing environment, utilising the Linux-cluster system at the Leibniz Rechenzentrum, Garching.

Murine primary crypt isolation and intestinal organoid culture. Murine intestinal crypts were isolated following digestion with EDTA (30 min; 4°C) and mechanical dissociation. The supernatant was filtered through a 70µm cell strainer, pelleted by centrifugation, and resuspended in Matrigel (BD Biosciences). 25µl Matrigel®-organoid domes were plated in 48-well plates (Eppendorf) together with 250µl IntestiCult™ Organoid Growth Medium (STEMCELL Technologies) and maintained in a humidified 5% CO_2 atmosphere at 37°C. Organoids were passaged every 7 days by mechanical disruption using a 1ml syringe with a 20G needle, pelleted by centrifugation, and embedded in fresh Matrigel.

Induction of *ex vivo* recombination and fatty acid stimulation of intestinal organoids. Intestinal organoids from nATF6 Vil-Cre^{ERT2} (fl/fl^{ERT2} and tg/tg^{ERT2}) were passaged three days before the start of the experiment and cultivated in self-made crypt culture medium (CCM;

advanced DMEM/F12 medium (Gibbco), 2mM GlutaMax (Gibbco), 10mM HEPES, penicillin, streptomycin and amphotericin (all Sigma-Aldrich) supplemented with N2, B27 (both Gibbco), 1mM N-acetylcysteine (Sigma-Aldrich), 50ng/ml EGF (ImmunoTools), 100ng/ml noggin and 0.5µg/ml R-spondin 1 (both PeproTec)). *ATF6* overexpression in intestinal organoids was induced by adding 500nM (Z)-4-hydroxytamoxifen (4-OHT; LKT) to the culture medium for 24h. After induction, organoids were exposed to Eicosanoic 20,20,20-D3 acid (30µM; Larodan) in CCM for 24h. Organoids were subsequently harvested in 0.2% SDS in ddH_20.

Fatty acid analyses. For FA quantification in mouse tissues and investigation of eicosanoic acid elongation in organoids, FA methyl esters (FAMEs) were generated by acetyl chloride and methanol treatment, and extracted with hexan [96]. Total FA analysis was carried out using a Shimadzu 2010 GC-MS system (Duisburg, Germany). FAMEs were separated on a BPX70 column (10 m length, 0.10 mm diameter, 0.20 µm film thickness) from SGE using helium as the carrier gas. The initial oven temperature was 50°C and was programed to increase at 40°C/min to 155°C, 6°C/min to 210°C, and finally 15°C/min to 250°C. D3-eicosanoic acid and its elongation products in organoids were quantified by single-ion monitoring of specific fragment ions (D3-eicosanoic acid, 329 m/z; D3-docosanoic acid, 357 m/z). The internal standard was C21:0-iso.

Statistical analysis. Statistical analyses were carried out using R (R software foundation, Vienna, Austria) or GraphPad Prism (version 9.00; GraphPad Software, San Diego, CA, USA). For comparing the mean of two groups, unpaired student's T-test or Wilcoxon test was used where appropriate. Differences between multiple groups were tested using ANOVA or Kruskal-Wallis tests. For testing differences in frequency, Fisher's exact test was used. Effect sizes were determined using the effsize R package, employing Cohen's d, calculated as the mean difference divided by the standard deviation for each pairwise difference. To test for differences in beta diversity, multivariate statistical testing was conducted using Permutational multivariate analysis of variance (PERMANOVA) [97]. Trends in spatial data were detected using locally estimated scatterplot smoothing (LOESS), as implemented in the stat_smooth function of ggplot2 [90]. For hierarchical clustering of metabolite intensities, Ward's method was used [98]. Multiple comparisons were controlled using the method of Benjamini & Hochberg [99]. Unless otherwise specified all data are presented as the mean ± standard deviation, *p*-values < 0.05 are considered statistically significant ($p<0.05$=*, $p<0.01$=**, $p<0.01$=***, $p<0.001$=****).

Figure legends

Fig. 1: High ATF6 expression defines a subset of CRC patients and associates with CRC-enriched bacterial genera.

a, QuPath quantified ATF6 H-score of nuclear (NUC) and cytoplasmic (CYT) ATF6 expression in immunohistochemically stained CRC patient tissue samples (cohort 1). Representative images of ATF6-high and ATF6-low staining in the tumor centre (TC) and the invasive front (IF). Percentage shows subpopulation of CRC patients in each ATF6-stained category (ATF6-low, light red; ATF6-high, dark red). Scale bars: 300µm overview, 50µm zoom-in. **b,** Classification model of ATF6 H-scores quantified using QuPath (true labels) versus ATF6 H-scores predicted by the classification algorithm (predicted labels) for ATF6-high and ATF6-low CRC patients. **c,** Pie chart showing percentage of ATF6-high and ATF6-low CRC patients identified in CRC cohort 2 using the classification model. **d,** Regression model of ATF6 H-scores quantified using QuPath (true values) versus ATF6 H-scores predicted by the regression algorithm (predicted values) for nuclear (NUC) and cytoplasmic (CYT) ATF6 expression. **e,** Pie chart showing percentage of ATF6-high and ATF6-low CRC patients identified in CRC cohort 2 using the regression model. **f,** QuPath quantified ATF6 H-score of nuclear (NUC) and cytoplasmic (CYT) ATF6 expression in immunohistochemically stained CRC patient tissue samples (cohort 3, LOCRC). Representative images of ATF6-high and ATF6-low staining. Percentage shows subpopulation of CRC patients in each ATF6-stained category. Scale bars: 300µm overview, 50 µm zoom-in. **g,** QuPath quantified ATF6 H-score of nuclear (NUC) and cytoplasmic (CYT) ATF6 expression in immunohistochemically stained CRC patient tissue samples (cohort 3, EOCRC). Representative images of ATF6-high and ATF6-low staining. Percentage shows subpopulation of CRC patients in each ATF6-stained category. Scale bars: 300µm overview, 50µm zoom-in. **h,** Plot of ATF6 activity in CRC patients (TCGA Database) when bacterial genus is present (x-axis) and the significance (y-axis). Marked in orange/red are those genera significantly associated with ATF6 activity, with red dots representing classical CRC-associated genera. **i,** Plot of ATF6 activity in CRC patients (TCGA Database) when bacteria are absent (grey) or present (red) for the CRC-associated genera marked red in h.

Fig. 2: High ATF6 expression defines a subset of CRC patients and associates with CRC-enriched bacterial genera.

a, Survival curve showing percent survival of fl/fl, tg/wt, tg/tg specific pathogen-free (SPF) and tg/tg germ-free (GF) mice between 0-25 weeks of age. **b,** Tumor incidence (percentage) of SPF fl/fl, tg/wt and tg/tg mice and GF tg/tg mice at the pre-tumor (5wk), tumor (12wk) and late-tumor (15+wk) time points. Grey represents no tumor, red represents tumor. **c,** Mean

generalized UniFrac distance relative to control across fl/fl, tg/wt and tg/tg samples. **d,** Correlation between relative expression, as measured by qPCR (2-ΔΔCt), of *Grp78* and community diversity metrics (Shannon Effective and Mean Generalized Unifrac Distance). **e,** Spearman's rank correlation between Shannon Effective and tumor number. **f,** ROC curves comparing classification accuracy of Random Forest (RF), LASSO (L) and Ridge (R) regression models built on luminal and mucosal data, respectively. Mucosal data was randomly subsampled to match luminal sample size (total n=63, random subsample=54). Models were trained using repeated 5-fold cross-validation (CV). **g,** Heatmap of early change (EC), sustained change (SC) and late change (LC) abundances at 5 and 12- weeks in fl/fl and tg/tg mice. Grey represents non-tumor, red represents tumor. Marked with an asterisk are those ASVs that were identified as CRC-enriched genera correlating with ATF6 activity in CRC patients (Fig. 1h). **h,** Tumor incidence (percentage) by spatially resolved site from proximal to distal colon. Mean Shannon Effective diversity at each site along the colon in fl/fl mice (top) and tg/tg mice (bottom). Magnitude of change between genotypes by site (Cohen's d effect size). **i,** Mucosal alpha diversity (Shannon Effective) in fl/fl controls (CTRL) and tg/tg mice across the three mucosal phenotypes: Non-tumor (NT), Tumor-adjacent (TA) and Tumor (T). **j,** metaNMDS plot of beta diversity, based on generalized UniFrac distance comparing mucosa from fl/fl mice (CTRL) to Non-tumor (NT), Tumor-adjacent (TA) and tumor (T) mucosa from tg/tg mice.

Fig. 3: ATF6 transcriptional response alters colonic metabolism and links fatty acid biosynthesis to the presence of bacteria

a, Schematic of non-tumor (NT) and tumor (T) phenotypes associated with GF and SPF fl/fl (n=6 and n=6, respectively) and tg/tg (n=6 and n=7, respectively) mice, highlighting the genotypes and colonization status used for the RNA sequencing analyses (blue box and arrow). Created with BioRender.com. **b,** Volcano plot of detected genes in fl/fl versus tg/tg nATF6^{IEC} mice showing the number and percentage of genes that are unchanged (No Change), upregulated in tg/tg mice (UP) or downregulated in tg/tg mice (DOWN). Threshold: -0.5 > log2FC >0.5, *p* adj. <0.05. **c,** Lollipop graph of the top and bottom regulated KEGG pathways in tg/tg versus fl/fl nATF6^{IEC} SPF mice (*p* adj. <= 0.25, −1 =>NES>= 1, with a minimum of 50% of genes detected in the pathway). Metabolic pathways are highlighted in blue. NES, normalized enrichment score. **d,** Alluvial plot depicting the flows used to define SiRCle clusters in a comparison between SPF and GF mice. Each data type (SPF and GF) has been labelled as a column, with one of three states (UP, No Change, DOWN) defined for each column based on the results for differential analysis between fl/fl versus tg/tg in that data type. Shown are the flows between each data type and state, which define the regulatory clusters (third column). The number and percentage of genes in the flow are depicted next to each regulatory cluster. **e,** Volcano Plot of genes in the regulatory cluster Core-ATF6 UP. **f,**

Volcano Plot of genes in the regulatory cluster SPF UP. Genes related to fatty acid metabolism are highlighted in blue. **g,** Volcano plot of detected genes in fl/fl (n=5) versus tg/tg (n=7) nATF6 Vil-Cre^{ERT2} SPF mice following acute activation of ATF6, showing the number and percentage of genes that are unchanged (No Change), upregulated in tg/tg mice (UP) or downregulated in tg/tg mice (DOWN). Threshold: -0.5 > log2FC >0.5, *p* adj. <0.05. Genes related to fatty acid metabolism are highlighted in blue.

Fig. 4: Inhibition of FASN prevents tumor formation in tg/tg nATF6^{IEC} mice

a, Representative images of low H-score and high H-score FASN immunohistochemically stained in CRC patient tissue samples (cohort 1). Scale bars: 300µm overview, 50µm zoom-in. **b,** QuPath quantified FASN H-score with patients grouped into ATF6-low and ATF6-high (according to QuPath quantified ATF6 H-score). **c,** Kaplan-Meier analysis of disease-free survival of patients in the Pan-Cancer Atlas database (*n=10.967* cases including approx. 600 CRC cases) with patients grouped into FASN+ATF6 unaltered, ATF6-only amp/gain or ATF6+FASN amp/gain. **d,** Kaplan-Meier analysis of disease-free survival of patients in The Cancer Genome Atlas database (TCGA; *n=640* CRC cases) with patients grouped into FASN+ATF6 unaltered, ATF6-only amp/gain or ATF6+FASN amp/gain. **e,** Schematic showing the experimental design for in vivo C75 FASN inhibitor intervention. SPF mice were intraperitoneally (i.p.) injected either with the RPMI control or the C57 FASN inhibitor bi-weekly from the age of 3 weeks. After an intervention period of 9 weeks, mice were sacrificed at 12 weeks of age. Arrows indicate i.p. injections. **f,** Tumor incidence (percentage) of SPF fl/fl and tg/tg mice after termination of the intervention with either RPMI (controls) or C75 FASN inhibitor. Grey represents no tumor, red represents tumor. Each bar shows the number of mice for each genotype. **g,** Representative macroscopic images of the colon of the tg/tg genotype on RPMI or C75. Marked with circles and asterisks are tumors identified in the control group. **h,** Tumor number in SPF fl/fl and tg/tg mice after invervention with RPMI or C75. **i,** Tumor volume in SPF fl/fl and tg/tg mice after intervention with RPMI or C75. **j,** Differentially abundant taxa between RPMI and C75 treated mice as determined by LEfSe analysis, ranked by LDA score (LDA threshold = 3.0).

Fig.5: ATF6-enriched LCFAs drive a bacterial lipid-response signature

a, Boxplots of microbiota-correlated Long-chain fatty acids in fl/fl and tg/tg mice at the 5wk, 12wk and 20wk time points. b, Spearman's rank correlation networks of microbiota-correlated fatty acid species, clr-transformed EC/SC taxa abundances and community metrics using a correlation threshold (r) of 0.5, at the 5wk time point in tg/tg mice. **c,** Percentage of saturated fatty acids (SAFA) in NT and T tissue after quantification of total FA using GC-MS. **d,** Percentage of SAFA plotted against tumor number after quantification of total FA using GC-MS. **e,** Quantification of FA22:0 to FA20:0 (ratio) after quantification of total FA using GC-MS.

f, Representative images of intestinal organoids on day 1 (d1) and day 7 (d7) after culture, for the fl/fl and tg/tg genotype. Scale bars: 50µm. **g,** Quantification of organoid size as the sum of two dimensions in µm at d1 and d7 for the fl/fl and tg/tg genotype. **h,** Quantification of the number of crypts per cyst at d7 for the fl/fl and the tg/tg genotype. **i,** Scheme showing the treatment of intestinal organoids from nATF6 Vil-Cre^{ERT2} (fl/fl^{ERT2} and tg/tg^{ERT2}) mice cultured *ex vivo*. Organoids were passaged at D0, *ATF6* expression was induced at D3 with 500nM (Z)-4-hydroxytamoxifen (4-OHT), and treated with D_3-FA 20:0 at D4, before harvesting at D5. Created with BioRender.com. **j,** Quantification of FA elongation as measured by the percentage of metabolized FA20:0 to FA22:0 in fl/fl^{ERT2} and tg/tg^{ERT2} mice. **k,** Spatial maps of Log10 transformed relative abundance of oleate hydratase (*ohyA)* positive ASVs along the entire colon in fl/fl and tg/tg mice. Marked is the susceptible and non-susceptible regions. **l,** Relative abundance of *ohyA* in fl/fl and tg/tg mice. **m,** Ratio of *ohyA* positive to *ohyA* negative taxa across various mucosal phenotypes in fl/fl and tg/tg mice. **n,** Spatial maps of Log10 transformed relative abundance of FA efflux pump (*farE*) positive ASVs along the entire colon in fl/fl and tg/tg mice. Marked is the susceptible and non-susceptible regions. **o,** Relative abundance of *farE* in fl/fl and tg/tg mice. **p,** Ratio of *farE* positive to *farE* negative taxa across various mucosal phenotypes in fl/fl and tg/tg mice.

Extended Data Fig. 1: ATF6 classification, training validation and correlation with MSI status in CRC patients

a, Nuclear (NUC) cutoff for the ATF6 H-score as determined using the online *Cutoff Finder* Web Application for Biomarker cutoff optimization, dividing patients into ATF6-high and ATF6-low. **b,** Cytoplasmic (CYT) cutoff for the ATF6 H-score as determined using the online *Cutoff Finder* Web Application for Biomarker cutoff optimization, dividing patients into ATF6-high and ATF6-low. **c,** Plot showing the classification model training accuracy, displaying the mean training and validation accuracy and their standard deviation. **d,** Plot showing the classification model training loss, displaying the mean training and validation loss and their standard deviation. **e,** Association of ATF6 activity with CRC-enriched genera after correcting for MSI status, and correlation of the CRC-enriched genera (highlighted in red, 1-5) with ATF6 activity for MSS and MSI in the absence and presence of the respective bacteria.

Extended Data Fig. 2: Monoallelic activation of nATF6 alters the colonic mucosal microbiota and biallelic activation licenses widespread expansion of driver taxa

a, Species Richness, Shannon Effective diversity, Faith's phylogenetic diversity at 5wk, 12wk and 20wk in fl/fl and tg/wt mice. **b,** Beta diversity, based on generalized UniFrac distance at 5wk, 12wk and 20wk between tg/wt and fl/fl mice. **c,** Precision-Recall curves from the Random Forest, L1-penalised Lasso and Ridge regression models built on luminal and mucosal data. Mucosal data was randomly subsampled to match luminal sample size (total n=63, random

subsample=54). d, Comparison of AUCROC values for each model trained, comparing luminal and mucosal datasets. **e,** Site-by-site comparison of the top five differentially abundant taxa between genotypes as determined by LEfSe analysis, ranked by LDA score (LDA threshold = 3.0). **f,** Spatial maps comparing Log10 transformed mean absolute abundance of EC/SC taxa between fl/fl and tg/tg mice, showing ASV_21; *Lactobacillus*, ASV_168; *Odoribacter* and ASV_7; *Mucispirillum*. The distribution amongst all mice is shown underneath, using LOESS regression to visualise trends. Individual fl/fl samples are shown in grey, while tg/tg samples are shown in pink. Circles define non-tumor (NT) tissue and triangles define tumor (T) tissue.

Extended Data Fig. 3: Minimal bacterial consortium colonization and fecal microbiota transplantation with CRC patient stool induces tumors in tg/tg mice

a, Survival curve showing percent survival of fl/fl, tg/wt, tg/tg mice following *M. schaedleri* monocolonization, OMM^{12} colonization or *M. schaedleri*+OMM^{12} colonization in weeks after gavage. **b,** Tumor incidence (percentage) of fl/fl, tg/wt and tg/tg mice following *M. schaedleri* monocolonization, OMM^{12} colonization or *M. schaedleri*+OMM^{12} colonization. White indicates non-tumor (NT), grey non-responder (NR) and red responder (R). Numbers indicate the biological replicates for each genotype and group. **c,** Tumor number of fl/fl, tg/wt and tg/tg mice following *M. schaedleri* monocolonization, OMM^{12} colonization or *M. schaedleri*+OMM^{12} colonization. Black indicates non-tumor (NT), grey non-responder (NR) and red responder (R). **d,** Inflammation score of fl/fl, tg/wt and tg/tg mice following *M. schaedleri* monocolonization, OMM^{12} colonization or *M. schaedleri*+OMM^{12} colonization. Black indicates non-tumor (NT), grey non-responder (NR) and red responder (R). **e,** Dysplasia score of fl/fl, tg/wt and tg/tg mice following *M. schaedleri* monocolonization, OMM^{12} colonization or *M. schaedleri*+OMM^{12} colonization. Black indicates non-tumor (NT), grey non-responder (NR) and red responder (R). **f,** Survival curve showing percent survival of fl/fl, tg/wt and tg/tg mice following colonization with stool from CRC patient 1 (green) and CRC patient 2 (yellow) in weeks after gavage. **g,** Tumor incidence (percentage) of fl/fl, tg/wt and tg/tg mice following colonization with stool from CRC patient 1 (green) and CRC patient 2 (yellow). Grey indicates non-tumor (NT) and red indicates tumor (T). **h,** Tumor number of fl/fl, tg/wt and tg/tg mice following colonization with stool from CRC patient 1 (green) and CRC patient 2 (yellow). **i,** Beta diversity showing the CRC donors (circled in black) and FMT mouse recipients for each donor (CRC1 green and CRC2 yellow), divided into T (dark) and NT (light) mice.

Extended Data Fig. 4: Germ-free tg/tg mice show altered metabolic pathways but do not show differential regulation our identified FA metabolism genes.

a, Volcano plot of detected genes in fl/fl versus tg/tg $nATF6^{IEC}$ GF mice showing the number and percentage of genes that are unchanged (No Change), upregulated in tg/tg mice (UP) or

downregulated in tg/tg mice (DOWN). Threshold: -0.5 > log2FC >0.5, *p* adj. <0.05. **b,** Lollipop graph of the top regulated KEGG pathways in tg/tg versus fl/fl nATF6^{IEC} GF mice (*p* adj. <= 0.25, −1 =>NES>= 1, with a minimum of 50% of genes detected in the pathway). Metabolic pathways are highlighted in blue. NES, normalized enrichment score. **c,** Volcano Plot of genes in the regulatory cluster CORE-ATF6 DOWN. **d,** Lollipop graph of the FA metabolism related genes from the SPF UP cluster (blue) shown for GF (grey) and SPF (red) mice. **e,** Volcano Plot of genes in the regulatory cluster SPF DOWN.

Extended Data Fig. 5: ATF6 and FASN upregulation show co-occurrence in CRC patients with survival not affected by ATF6 expression levels

a, Table showing the analysis of *ATF6* amplifications/gain and *FASN* amplifications/gain in the pan-cancer and TCGA Datasets, indicating the log2 odds ratio (OR), p value and observed association/tendency. **b,** Kaplan-Meier analysis of disease-free survival shown for ATF6-low (blue) and ATF6-high (red) at different months after surgery in CRC cohort 1. **c,** Kaplan-Meier analysis of overall survival shown for ATF6-low (green) and ATF6-high (blue) at different months after surgery in CRC cohort 3 EOCRC patients. **d,** Kaplan-Meier analysis of overall survival shown for ATF6-low (green) and ATF6-high (blue) at different months after surgery in CRC cohort 3 LOCRC patients. **e,** Kaplan-Meier analysis of overall survival of patients in the Pan-Cancer Atlas database (*n=10.967* cases including approx. 600 CRC cases) with patients grouped into FASN+ATF6 unaltered, ATF6-only amp/gain or ATF6+FASN amp/gain. **f,** Kaplan-Meier analysis of disease-free survival of patients in The Cancer Genome Atlas database (TCGA; *n=640* CRC cases) with patients grouped into FASN+ATF6 unaltered, ATF6-only amp/gain or ATF6+FASN amp/gain.

Extended Data Fig. 6: The pre-tumor tg/tg metabolite environment is enriched in lipids and depleted in amino acids and peptides, with tumor-associated taxa linking to lipids

a, PCA of metabolite profiles comparing fl/fl (circles), tg/wt (squares) and tg/tg (triangles) mice at 5wk, 12wk and 20wk. Blue indicates non-tumor (NT) and red tumor (T). **b,** Volcano plot of differentially enriched metabolites between fl/fl and tg/tg mice across all time points (Log2 fold change threshold = 2.0, *p*-value threshold = 0.05). **c,** PCA of luminal lipid profiles between tumor-susceptible/tumor (T) and non-tumor (NT) mice at 5wk, 12wk and 20wk. **d,** Heatmap of scaled differentially enriched metabolites, sorted by genotype and age. Rows are clustered using Ward's method. **e,** Circos plot of highly correlated ($r \geq 0.7$) features between blocks. The ASV block is depicted in red, while the metabolome block is shown in light blue. Orange lines indicate a positive correlation. The height of the line surrounding the plot indicates the group (NT in blue or T in red) which a given feature is associated with. **f,** Loadings plots of the top 30

annotated highly correlated features discriminating tumor from non-tumor, showing ASVs (left) and metabolites (right). Features are sorted by importance.

Extended Data Fig. 7: Microbial adaptation to the altered lipid environment

a, Volcano plot of differentially abundant pathways (log2 fold-change 0.32, adjusted *p*-value <0.05) predicted by PICRUSt2 comparing 5wk (pre-tumor) and 12wk (tumor) time points (left) in tg/tg mice and non-tumor controls to tumor-bearing mice (right). Pathways related to fatty acid metabolism are highlighted in blue. **b,** Heatmap of bacterial FA-response genes predicted by PICRUSt2 for fl/fl controls and non-tumor (NT), tumor-adjacent (TA) and tumor (T) mucosal phenotypes of tg/tg mice. Spatial sites along the colon and biological replicates (mouse) are numerically labelled underneath. **c,** Pie Charts depicting the genus contribution (indicated in percent) to *ohyA* abundance in NT, TA and T mucosal phenotypes of tg/tg mice. **d,** Pie Charts depicting the genus contribution (indicated in percent) to *farE* abundance in NT, TA and T mucosal phenotypes of tg/tg mice.

References

1 Braakman, I. & Bulleid, N. J. Protein folding and modification in the mammalian endoplasmic reticulum. *Annu Rev Biochem* **80**, 71-99, doi:10.1146/annurev-biochem-062209-093836 (2011).

2 Jacquemyn, J., Cascalho, A. & Goodchild, R. E. The ins and outs of endoplasmic reticulum-controlled lipid biosynthesis. *EMBO Rep* **18**, 1905-1921, doi:10.15252/embr.201643426 (2017).

3 Rutkowski, D. T. & Kaufman, R. J. A trip to the ER: coping with stress. *Trends Cell Biol* **14**, 20-28 (2004).

4 Shen, J., Chen, X., Hendershot, L. & Prywes, R. ER stress regulation of ATF6 localization by dissociation of BiP/GRP78 binding and unmasking of Golgi localization signals. *Dev Cell* **3**, 99-111 (2002).

5 Yoshida, H., Matsui, T., Yamamoto, A., Okada, T. & Mori, K. XBP1 mRNA is induced by ATF6 and spliced by IRE1 in response to ER stress to produce a highly active transcription factor. *Cell* **107**, 881-891 (2001).

6 Kaser, A. *et al.* XBP1 links ER stress to intestinal inflammation and confers genetic risk for human inflammatory bowel disease. *Cell* **134**, 743-756, doi:10.1016/j.cell.2008.07.021 (2008).

7 Bertolotti, A. *et al.* Increased sensitivity to dextran sodium sulfate colitis in IRE1beta-deficient mice. *J Clin Invest* **107**, 585-593, doi:10.1172/JCI11476 (2001).

8 Shkoda, A. *et al.* Interleukin-10 blocked endoplasmic reticulum stress in intestinal epithelial cells: impact on chronic inflammation. *Gastroenterology* **132**, 190-207, doi:10.1053/j.gastro.2006.10.030 (2007).

9 Stengel, S. T. *et al.* Activating Transcription Factor 6 Mediates Inflammatory Signals in Intestinal Epithelial Cells Upon Endoplasmic Reticulum Stress. *Gastroenterology* **159**, 1357-1374 e1310, doi:10.1053/j.gastro.2020.06.088 (2020).

10 Hanaoka, M. *et al.* Expression of ATF6 as a marker of pre-cancerous atypical change in ulcerative colitis-associated colorectal cancer: a potential role in the management of dysplasia. *J Gastroenterol*, doi:10.1007/s00535-017-1387-1 (2017).

11 Coleman, O. I. *et al.* Activated ATF6 Induces Intestinal Dysbiosis and Innate Immune Response to Promote Colorectal Tumorigenesis. *Gastroenterology* **155**, 1539-1552 e1512, doi:10.1053/j.gastro.2018.07.028 (2018).

12 Waldschmitt, N. *et al.* C/EBP homologous protein inhibits tissue repair in response to gut injury and is inversely regulated with chronic inflammation. *Mucosal immunology* **7**, 1452-1466, doi:10.1038/mi.2014.34 (2014).
13 Lee, A. S. Glucose-regulated proteins in cancer: molecular mechanisms and therapeutic potential. *Nat Rev Cancer* **14**, 263-276, doi:10.1038/nrc3701 (2014).
14 Lin, Y. H. *et al.* Multiple gene expression classifiers from different array platforms predict poor prognosis of colorectal cancer. *Clin Cancer Res* **13**, 498-507, doi:10.1158/1078-0432.Ccr-05-2734 (2007).
15 Schewe, D. M. & Aguirre-Ghiso, J. A. ATF6alpha-Rheb-mTOR signaling promotes survival of dormant tumor cells in vivo. *Proc Natl Acad Sci U S A* **105**, 10519-10524, doi:10.1073/pnas.0800939105 (2008).
16 Wu, X. *et al.* A missense polymorphism in ATF6 gene is associated with susceptibility to hepatocellular carcinoma probably by altering ATF6 level. *Int J Cancer* **135**, 61-68, doi:10.1002/ijc.28649 (2014).
17 Cifkova, E. *et al.* Determination of lipidomic differences between human breast cancer and surrounding normal tissues using HILIC-HPLC/ESI-MS and multivariate data analysis. *Anal Bioanal Chem* **407**, 991-1002, doi:10.1007/s00216-014-8272-z (2015).
18 Eggers, L. F. *et al.* Lipidomes of lung cancer and tumour-free lung tissues reveal distinct molecular signatures for cancer differentiation, age, inflammation, and pulmonary emphysema. *Sci Rep* **7**, 11087, doi:10.1038/s41598-017-11339-1 (2017).
19 Rohrig, F. & Schulze, A. The multifaceted roles of fatty acid synthesis in cancer. *Nat Rev Cancer* **16**, 732-749, doi:10.1038/nrc.2016.89 (2016).
20 Coleman, O., Ecker, M. & Haller, D. Dysregulated lipid metabolism in colorectal cancer. *Curr Opin Gastroenterol* **38**, 162-167, doi:10.1097/MOG.0000000000000811 (2022).
21 Porstmann, T. *et al.* SREBP activity is regulated by mTORC1 and contributes to Akt-dependent cell growth. *Cell Metab* **8**, 224-236, doi:10.1016/j.cmet.2008.07.007 (2008).
22 Zaytseva, Y. Y. *et al.* Cancer cell-associated fatty acid synthase activates endothelial cells and promotes angiogenesis in colorectal cancer. *Carcinogenesis* **35**, 1341-1351, doi:10.1093/carcin/bgu042 (2014).
23 Zaytseva, Y. Y. *et al.* Inhibition of fatty acid synthase attenuates CD44-associated signaling and reduces metastasis in colorectal cancer. *Cancer Res* **72**, 1504-1517, doi:10.1158/0008-5472.CAN-11-4057 (2012).
24 Ecker, J. *et al.* The Colorectal Cancer Lipidome: Identification of a Robust Tumor-Specific Lipid Species Signature. *Gastroenterology* **161**, 910-923 e919, doi:10.1053/j.gastro.2021.05.009 (2021).
25 Zeng, L. *et al.* ATF6 modulates SREBP2-mediated lipogenesis. *EMBO J* **23**, 950-958, doi:10.1038/sj.emboj.7600106 (2004).
26 Howarth, D. L. *et al.* Activating transcription factor 6 is necessary and sufficient for alcoholic fatty liver disease in zebrafish. *PLoS Genet* **10**, e1004335, doi:10.1371/journal.pgen.1004335 (2014).
27 Chen, X. *et al.* Hepatic ATF6 Increases Fatty Acid Oxidation to Attenuate Hepatic Steatosis in Mice Through Peroxisome Proliferator-Activated Receptor alpha. *Diabetes* **65**, 1904-1915, doi:10.2337/db15-1637 (2016).
28 Jesinghaus, M. *et al.* Morphology Matters: A Critical Reappraisal of the Clinical Relevance of Morphologic Criteria From the 2019 WHO Classification in a Large Colorectal Cancer Cohort Comprising 1004 Cases. *Am J Surg Pathol* **45**, 969-978, doi:10.1097/PAS.0000000000001692 (2021).
29 Bankhead, P. *et al.* QuPath: Open source software for digital pathology image analysis. *Sci Rep* **7**, 16878, doi:10.1038/s41598-017-17204-5 (2017).
30 Dohlman, A. B. *et al.* The cancer microbiome atlas: a pan-cancer comparative analysis to distinguish tissue-resident microbiota from contaminants. *Cell Host Microbe* **29**, 281-298 e285, doi:10.1016/j.chom.2020.12.001 (2021).

1210 31 Eberl, C. *et al.* Reproducible Colonization of Germ-Free Mice With the Oligo-Mouse-Microbiota
1211 in Different Animal Facilities. *Front Microbiol* **10**, 2999, doi:10.3389/fmicb.2019.02999 (2019).
1212 32 Mora, A., Schmidt, C., Balderson, B., Frezza, C. & Bodén, M. SiRCle (Signature Regulatory
1213 Clustering) model integration reveals mechanisms of phenotype regulation in renal cancer.
1214 *bioRxiv*, 2022.2007.2002.498058, doi:10.1101/2022.07.02.498058 (2022).
1215 33 Zhu, L. *et al.* Germline Variants of CYBA and TRPM4 Predispose to Familial Colorectal Cancer.
1216 *Cancers (Basel)* **14**, doi:10.3390/cancers14030670 (2022).
1217 34 Lian, J., Nelson, R. & Lehner, R. Carboxylesterases in lipid metabolism: from mouse to human.
1218 *Protein Cell* **9**, 178-195, doi:10.1007/s13238-017-0437-z (2018).
1219 35 Thesseling, F. A. *et al.* Novel insights into oxidation of fatty acids and fatty alcohols by
1220 cytochrome P450 monooxygenase CYP4B1. *Arch Biochem Biophys* **679**, 108216,
1221 doi:10.1016/j.abb.2019.108216 (2020).
1222 36 Emterling, A. *et al.* Clinicopathological significance of Nup88 expression in patients with
1223 colorectal cancer. *Oncology* **64**, 361-369, doi:10.1159/000070294 (2003).
1224 37 Merkulova, M. *et al.* Mapping the H(+) (V)-ATPase interactome: identification of proteins
1225 involved in trafficking, folding, assembly and phosphorylation. *Sci Rep* **5**, 14827,
1226 doi:10.1038/srep14827 (2015).
1227 38 Chen, L. J. *et al.* IGF2BP3 promotes the progression of colorectal cancer and mediates
1228 cetuximab resistance by stabilizing EGFR mRNA in an m(6)A-dependent manner. *Cell Death Dis*
1229 **14**, 581, doi:10.1038/s41419-023-06099-y (2023).
1230 39 Zuo, S., Wu, L., Wang, Y. & Yuan, X. Long Non-coding RNA MEG3 Activated by Vitamin D
1231 Suppresses Glycolysis in Colorectal Cancer via Promoting c-Myc Degradation. *Front Oncol* **10**,
1232 274, doi:10.3389/fonc.2020.00274 (2020).
1233 40 Chu, C. M. *et al.* Gene expression profiling of colorectal tumors and normal mucosa by
1234 microarrays meta-analysis using prediction analysis of microarray, artificial neural network,
1235 classification, and regression trees. *Dis Markers* **2014**, 634123, doi:10.1155/2014/634123
1236 (2014).
1237 41 Duarte-Pereira, S. *et al.* Extensive regulation of nicotinate phosphoribosyltransferase (NAPRT)
1238 expression in human tissues and tumors. *Oncotarget* **7**, 1973-1983,
1239 doi:10.18632/oncotarget.6538 (2016).
1240 42 Gan, C. *et al.* Carboxylesterase 1 family knockout alters drug disposition and lipid metabolism.
1241 *Acta Pharm Sin B* **13**, 618-631, doi:10.1016/j.apsb.2022.10.017 (2023).
1242 43 Wang, L. *et al.* Antimicrobial activity of human islet amyloid polypeptides: an insight into
1243 amyloid peptides' connection with antimicrobial peptides. *Biological Chemistry* **393**, 641-646,
1244 doi:doi:10.1515/hsz-2012-0107 (2012).
1245 44 Douglas, G. M. *et al.* PICRUSt2 for prediction of metagenome functions. *Nat Biotechnol* **38**,
1246 685-688, doi:10.1038/s41587-020-0548-6 (2020).
1247 45 Caspi, R. *et al.* The MetaCyc database of metabolic pathways and enzymes and the BioCyc
1248 collection of Pathway/Genome Databases. *Nucleic Acids Res* **42**, D459-471,
1249 doi:10.1093/nar/gkt1103 (2014).
1250 46 Subramanian, C., Frank, M. W., Batte, J. L., Whaley, S. G. & Rock, C. O. Oleate hydratase from
1251 Staphylococcus aureus protects against palmitoleic acid, the major antimicrobial fatty acid
1252 produced by mammalian skin. *J Biol Chem* **294**, 9285-9294, doi:10.1074/jbc.RA119.008439
1253 (2019).
1254 47 Alnaseri, H. *et al.* Inducible Expression of a Resistance-Nodulation-Division-Type Efflux Pump
1255 in Staphylococcus aureus Provides Resistance to Linoleic and Arachidonic Acids. *J Bacteriol*
1256 **197**, 1893-1905, doi:10.1128/JB.02607-14 (2015).
1257 48 Bray, F. *et al.* Global cancer statistics 2018: GLOBOCAN estimates of incidence and mortality
1258 worldwide for 36 cancers in 185 countries. *CA Cancer J Clin* **68**, 394-424,
1259 doi:10.3322/caac.21492 (2018).
1260 49 Vriens, K. *et al.* Evidence for an alternative fatty acid desaturation pathway increasing cancer
1261 plasticity. *Nature* **566**, 403-406, doi:10.1038/s41586-019-0904-1 (2019).

1262 50 So, J. S. *et al.* Silencing of lipid metabolism genes through IRE1alpha-mediated mRNA decay
1263 lowers plasma lipids in mice. *Cell Metab* **16**, 487-499, doi:10.1016/j.cmet.2012.09.004 (2012).
1264 51 Sriburi, R. *et al.* Coordinate regulation of phospholipid biosynthesis and secretory pathway
1265 gene expression in XBP-1(S)-induced endoplasmic reticulum biogenesis. *J Biol Chem* **282**, 7024-
1266 7034, doi:10.1074/jbc.M609490200 (2007).
1267 52 Lee, A. H., Scapa, E. F., Cohen, D. E. & Glimcher, L. H. Regulation of hepatic lipogenesis by the
1268 transcription factor XBP1. *Science* **320**, 1492-1496, doi:10.1126/science.1158042 (2008).
1269 53 Bommiasamy, H. *et al.* ATF6alpha induces XBP1-independent expansion of the endoplasmic
1270 reticulum. *J Cell Sci* **122**, 1626-1636, doi:10.1242/jcs.045625 (2009).
1271 54 Mika, A. *et al.* Rearrangements of Blood and Tissue Fatty Acid Profile in Colorectal Cancer -
1272 Molecular Mechanism and Diagnostic Potential. *Front Oncol* **11**, 689701,
1273 doi:10.3389/fonc.2021.689701 (2021).
1274 55 Thomas, A. M. *et al.* Metagenomic analysis of colorectal cancer datasets identifies cross-cohort
1275 microbial diagnostic signatures and a link with choline degradation. *Nat Med* **25**, 667-678,
1276 doi:10.1038/s41591-019-0405-7 (2019).
1277 56 Wirbel, J. *et al.* Meta-analysis of fecal metagenomes reveals global microbial signatures that
1278 are specific for colorectal cancer. *Nat Med* **25**, 679-689, doi:10.1038/s41591-019-0406-6
1279 (2019).
1280 57 Dejea, C. M. *et al.* Patients with familial adenomatous polyposis harbor colonic biofilms
1281 containing tumorigenic bacteria. *Science* **359**, 592-597, doi:10.1126/science.aah3648 (2018).
1282 58 Kim, M. *et al.* Fecal Metabolomic Signatures in Colorectal Adenoma Patients Are Associated
1283 with Gut Microbiota and Early Events of Colorectal Cancer Pathogenesis. *mBio* **11**,
1284 doi:10.1128/mBio.03186-19 (2020).
1285 59 Yachida, S. *et al.* Metagenomic and metabolomic analyses reveal distinct stage-specific
1286 phenotypes of the gut microbiota in colorectal cancer. *Nat Med* **25**, 968-976,
1287 doi:10.1038/s41591-019-0458-7 (2019).
1288 60 Budczies, J. *et al.* Cutoff Finder: a comprehensive and straightforward Web application
1289 enabling rapid biomarker cutoff optimization. *PLoS One* **7**, e51862,
1290 doi:10.1371/journal.pone.0051862 (2012).
1291 61 Garcia-Alonso, L., Holland, C. H., Ibrahim, M. M., Turei, D. & Saez-Rodriguez, J. Benchmark and
1292 integration of resources for the estimation of human transcription factor activities. *Genome*
1293 *Res* **29**, 1363-1375, doi:10.1101/gr.240663.118 (2019).
1294 62 Kuznetsova, A., Brockhoff, P. B. & Christensen, R. H. B. lmerTest Package: Tests in Linear Mixed
1295 Effects Models. *Journal of Statistical Software* **82**, 1 - 26, doi:10.18637/jss.v082.i13 (2017).
1296 63 Benjamini, Y. & Hochberg, Y. Controlling the False Discovery Rate - a Practical and Powerful
1297 Approach to Multiple Testing. *J R Stat Soc B* **57**, 289-300, doi:DOI 10.1111/j.2517-
1298 6161.1995.tb02031.x (1995).
1299 64 Godon, J. J., Zumstein, E., Dabert, P., Habouzit, F. & Moletta, R. Molecular microbial diversity
1300 of an anaerobic digestor as determined by small-subunit rDNA sequence analysis. *Applied and*
1301 *environmental microbiology* **63**, 2802-2813 (1997).
1302 65 Salter, S. J. *et al.* Reagent and laboratory contamination can critically impact sequence-based
1303 microbiome analyses. *BMC Biol* **12**, 87, doi:10.1186/s12915-014-0087-z (2014).
1304 66 Tourlousse, D. M. *et al.* Synthetic spike-in standards for high-throughput 16S rRNA gene
1305 amplicon sequencing. *Nucleic Acids Research* **45**, doi:ARTN e23

1306 10.1093/nar/gkw984 (2017).
1307 67 Metwaly, A. *et al.* Integrated microbiota and metabolite profiles link Crohn's disease to sulfur
1308 metabolism. *Nat Commun* **11**, 4322, doi:10.1038/s41467-020-17956-1 (2020).
1309 68 Kozich, J. J., Westcott, S. L., Baxter, N. T., Highlander, S. K. & Schloss, P. D. Development of a
1310 dual-index sequencing strategy and curation pipeline for analyzing amplicon sequence data on
1311 the MiSeq Illumina sequencing platform. *Applied and environmental microbiology* **79**, 5112-
1312 5120, doi:10.1128/AEM.01043-13 (2013).

1313 69 Lagkouvardos, I. *et al.* IMNGS: A comprehensive open resource of processed 16S rRNA
1314 microbial profiles for ecology and diversity studies. *Sci Rep* **6**, 33721, doi:10.1038/srep33721
1315 (2016).
1316 70 Edgar, R. C. UPARSE: highly accurate OTU sequences from microbial amplicon reads. *Nat*
1317 *Methods* **10**, 996-998, doi:10.1038/nmeth.2604 (2013).
1318 71 Edgar, R. C. UNOISE2: improved error-correction for Illumina 16S and ITS amplicon sequencing.
1319 *bioRxiv*, 081257, doi:10.1101/081257 (2016).
1320 72 Altschul, S. F., Gish, W., Miller, W., Myers, E. W. & Lipman, D. J. Basic local alignment search
1321 tool. *J Mol Biol* **215**, 403-410, doi:10.1016/S0022-2836(05)80360-2 (1990).
1322 73 Wang, Q., Garrity, G. M., Tiedje, J. M. & Cole, J. R. Naive Bayesian classifier for rapid assignment
1323 of rRNA sequences into the new bacterial taxonomy. *Applied and environmental microbiology*
1324 **73**, 5261-5267, doi:10.1128/AEM.00062-07 (2007).
1325 74 Davis, N. M., Proctor, D. M., Holmes, S. P., Relman, D. A. & Callahan, B. J. Simple statistical
1326 identification and removal of contaminant sequences in marker-gene and metagenomics data.
1327 *Microbiome* **6**, 226, doi:10.1186/s40168-018-0605-2 (2018).
1328 75 Lagkouvardos, I., Fischer, S., Kumar, N. & Clavel, T. Rhea: a transparent and modular R pipeline
1329 for microbial profiling based on 16S rRNA gene amplicons. *PeerJ* **5**, e2836,
1330 doi:10.7717/peerj.2836 (2017).
1331 76 McMurdie, P. J. & Holmes, S. phyloseq: an R package for reproducible interactive analysis and
1332 graphics of microbiome census data. *PLoS One* **8**, e61217, doi:10.1371/journal.pone.0061217
1333 (2013).
1334 77 Faith, D. P. Conservation Evaluation and Phylogenetic Diversity. *Biol Conserv* **61**, 1-10, doi:Doi
1335 10.1016/0006-3207(92)91201-3 (1992).
1336 78 Chen, J. *et al.* Associating microbiome composition with environmental covariates using
1337 generalized UniFrac distances. *Bioinformatics* **28**, 2106-2113,
1338 doi:10.1093/bioinformatics/bts342 (2012).
1339 79 Segata, N. *et al.* Metagenomic biomarker discovery and explanation. *Genome Biology* **12**,
1340 doi:ARTN R60

1341 10.1186/gb-2011-12-6-r60 (2011).
1342 80 Nearing, J. T. *et al.* Microbiome differential abundance methods produce different results
1343 across 38 datasets. *Nature Communications* **13**, doi:ARTN 342

1344 10.1038/s41467-022-28034-z (2022).
1345 81 Wirbel, J. *et al.* Microbiome meta-analysis and cross-disease comparison enabled by the
1346 SIAMCAT machine learning toolbox. *Genome Biol* **22**, 93, doi:10.1186/s13059-021-02306-1
1347 (2021).
1348 82 Sidak, D., Schwarzerova, J., Weckwerth, W. & Waldherr, S. Interpretable machine learning
1349 methods for predictions in systems biology from omics data. *Front Mol Biosci* **9**, 926623,
1350 doi:10.3389/fmolb.2022.926623 (2022).
1351 83 Herp, S. *et al.* Mucispirillum schaedleri Antagonizes Salmonella Virulence to Protect Mice
1352 against Colitis. *Cell Host Microbe* **25**, 681-694 e688, doi:10.1016/j.chom.2019.03.004 (2019).
1353 84 Subramanian, A. *et al.* Gene set enrichment analysis: a knowledge-based approach for
1354 interpreting genome-wide expression profiles. *Proc Natl Acad Sci U S A* **102**, 15545-15550,
1355 doi:10.1073/pnas.0506580102 (2005).
1356 85 Liberzon, A. *et al.* Molecular signatures database (MSigDB) 3.0. *Bioinformatics* **27**, 1739-1740,
1357 doi:10.1093/bioinformatics/btr260 (2011).
1358 86 Kanehisa, M. & Goto, S. KEGG: kyoto encyclopedia of genes and genomes. *Nucleic Acids Res*
1359 **28**, 27-30, doi:10.1093/nar/28.1.27 (2000).
1360 87 Korotkevich, G. *et al.* Fast gene set enrichment analysis. *bioRxiv*, 060012, doi:10.1101/060012
1361 (2021).
1362 88 Morgan M, F. S., Gentleman R. GSEABase: Gene set enrichment data structures and methods.
1363 *R package version 1.62.0* (2023).

89 Blighe K, R. S., Lewis M. EnhancedVolcano: Publication-ready volcano plots with enhanced colouring and labeling. *R package version 1.18.0* (2023).
90 Wickham, H. *ggplot2: Elegant Graphics for Data Analysis*. (Springer-Verlag New York, 2016).
91 Tsugawa, H. *et al.* MS-DIAL: data-independent MS/MS deconvolution for comprehensive metabolome analysis. *Nat Methods* **12**, 523-526, doi:10.1038/nmeth.3393 (2015).
92 Wehrens, R. *et al.* Improved batch correction in untargeted MS-based metabolomics. *Metabolomics* **12**, 88, doi:10.1007/s11306-016-1015-8 (2016).
93 Rohart, F., Gautier, B., Singh, A. & Le Cao, K. A. mixOmics: An R package for 'omics feature selection and multiple data integration. *PLoS Comput Biol* **13**, e1005752, doi:10.1371/journal.pcbi.1005752 (2017).
94 Singh, A. *et al.* DIABLO: an integrative approach for identifying key molecular drivers from multi-omics assays. *Bioinformatics* **35**, 3055-3062, doi:10.1093/bioinformatics/bty1054 (2019).
95 Kuhn M, J. S., Cimentada J corrr: Correlations in R. (2022).
96 Ecker, J., Scherer, M., Schmitz, G. & Liebisch, G. A rapid GC-MS method for quantification of positional and geometric isomers of fatty acid methyl esters. *J Chromatogr B Analyt Technol Biomed Life Sci* **897**, 98-104, doi:10.1016/j.jchromb.2012.04.015 (2012).
97 Anderson, M. J. A new method for non-parametric multivariate analysis of variance. *Austral Ecol* **26**, 32-46, doi:DOI 10.1046/j.1442-9993.2001.01070.x (2001).
98 Ward, J. H. Hierarchical Grouping to Optimize an Objective Function. *Journal of the American Statistical Association* **58**, 236-244, doi:10.1080/01621459.1963.10500845 (1963).
99 Benjamini, Y. & Hochberg, Y. Controlling the False Discovery Rate: A Practical and Powerful Approach to Multiple Testing. *Journal of the Royal Statistical Society: Series B (Methodological)* **57**, 289-300, doi:10.1111/j.2517-6161.1995.tb02031.x (1995).

Fig.1

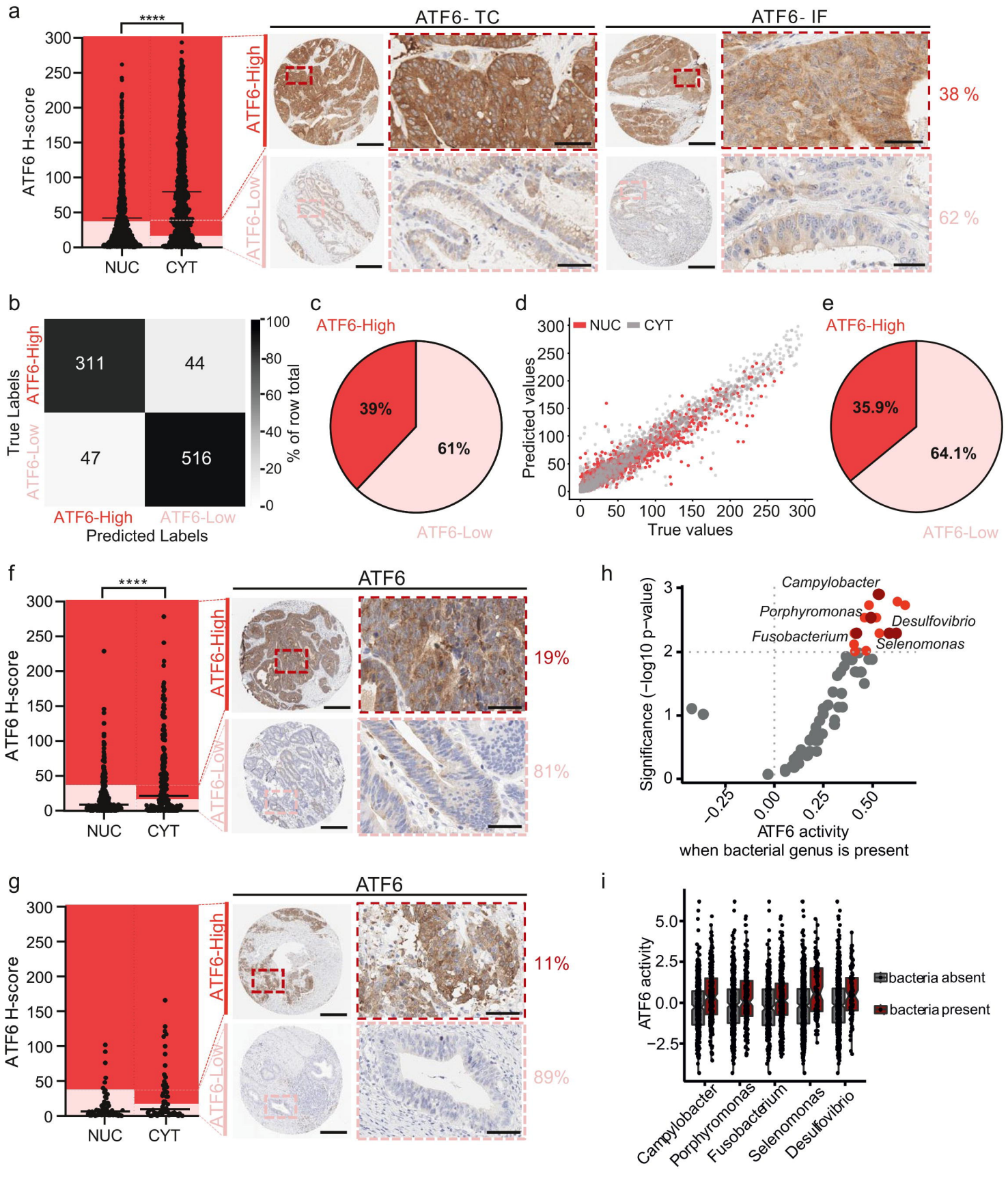
a
****
ATF6 H-score
NUC
CYT
ATF6- TC
ATF6- IF
ATF6-High
ATF6-Low
38 %
62 %
b
True Labels
ATF6-High
ATF6-Low
311
44
47
516
Predicted Labels
% of row total
c
ATF6-High
39%
61%
ATF6-Low
d
NUC
CYT
Predicted values
True values
e
ATF6-High
35.9%
64.1%
ATF6-Low
f
****
ATF6 H-score
NUC
CYT
ATF6
ATF6-High
ATF6-Low
19%
81%
h
Campylobacter
Porphyromonas
Fusobacterium
Desulfovibrio
Selenomonas
Significance (−log10 p−value)
ATF6 activity
when bacterial genus is present
g
ATF6 H-score
NUC
CYT
ATF6
ATF6-High
ATF6-Low
11%
89%
i
ATF6 activity
bacteria absent
bacteria present
Campylobacter
Porphyromonas
Fusobacterium
Selenomonas
Desulfovibrio

Fig.2

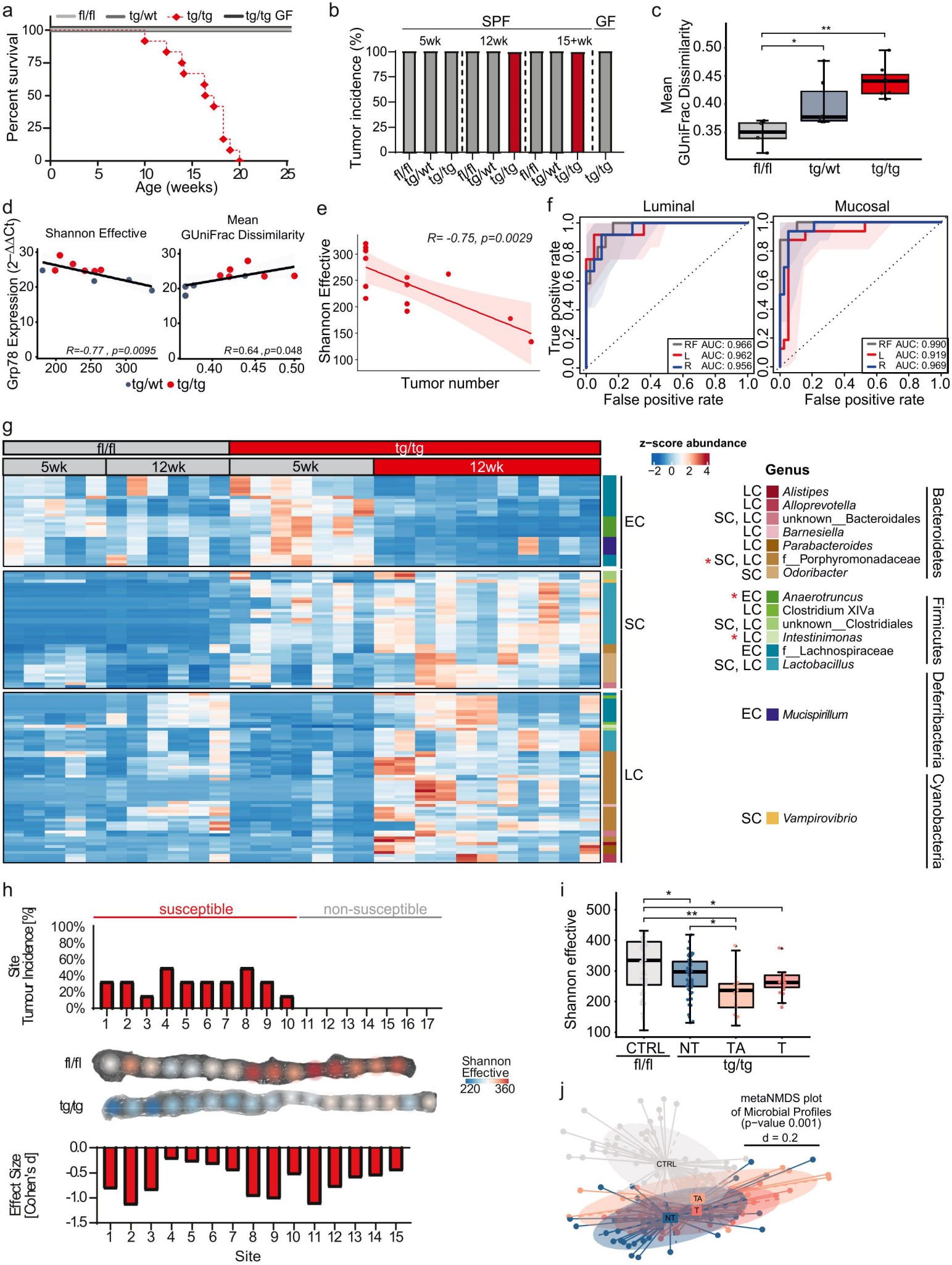
a
fl/fl
tg/wt
tg/tg
tg/tg GF
Percent survival
Age (weeks)
b
SPF
GF
5wk
12wk
15+wk
Tumor incidence (%)
c
Mean GUniFrac Dissimilarity
fl/fl
tg/wt
tg/tg
d
Shannon Effective
Mean GUniFrac Dissimilarity
Grp78 Expression (2−ΔΔCt)
R=-0.77 , p=0.0095
R=0.64 ,p=0.048
tg/wt
tg/tg
e
R= -0.75, p=0.0029
Shannon Effective
Tumor number
f
Luminal
Mucosal
True positive rate
False positive rate
RF AUC: 0.966
L AUC: 0.962
R AUC: 0.956
RF AUC: 0.990
L AUC: 0.919
R AUC: 0.969
g
fl/fl
tg/tg
5wk
12wk
EC
SC
LC
z−score abundance
Genus
LC Alistipes
LC Alloprevotella
SC, LC unknown__Bacteroidales
LC Barnesiella
LC Parabacteroides
* SC, LC f__Porphyromonadaceae
SC Odoribacter
Bacteroidetes
* EC Anaerotruncus
LC Clostridium XIVa
SC, LC unknown__Clostridiales
* LC Intestinimonas
EC f__Lachnospiraceae
SC, LC Lactobacillus
Firmicutes
EC Mucispirillum
Deferribacteria
SC Vampirovibrio
Cyanobacteria
h
susceptible
non-susceptible
Site Tumour Incidence [%]
fl/fl
tg/tg
Shannon Effective
220
360
Effect Size [Cohen's d]
Site
i
Shannon effective
CTRL
NT
TA
T
fl/fl
tg/tg
j
metaNMDS plot of Microbial Profiles (p−value 0.001)
d = 0.2
CTRL
TA
T
NT

Fig.3

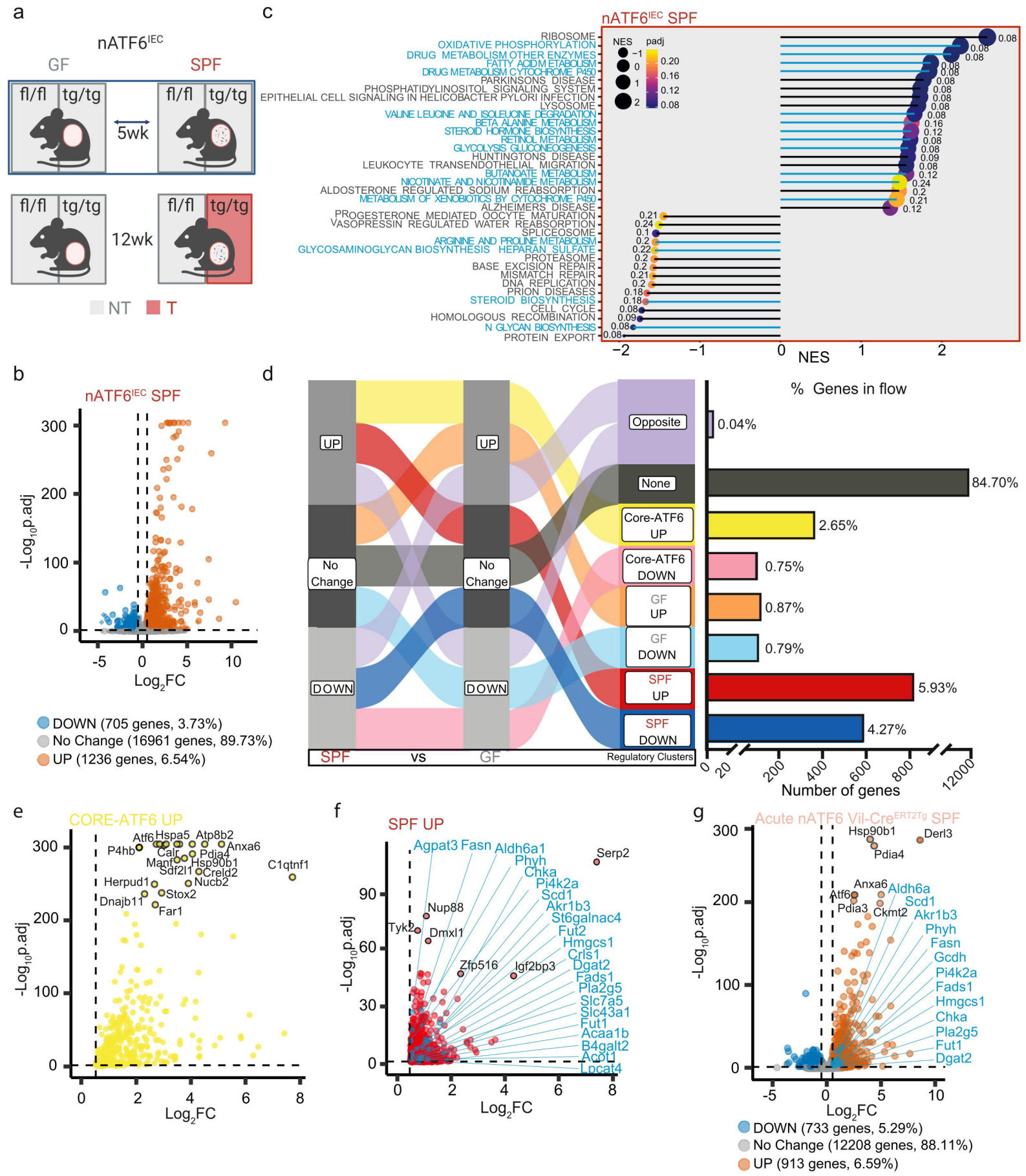
a
nATF6IEC
GF
SPF
fl/fl
tg/tg
5wk
12wk
NT
T
b
nATF6IEC SPF
-Log10p.adj
Log2FC
DOWN (705 genes, 3.73%)
No Change (16961 genes, 89.73%)
UP (1236 genes, 6.54%)
c
nATF6IEC SPF
NES
padj
RIBOSOME
OXIDATIVE PHOSPHORYLATION
DRUG METABOLISM OTHER ENZYMES
FATTY ACID METABOLISM
DRUG METABOLISM CYTOCHROME P450
PARKINSONS DISEASE
PHOSPHATIDYLINOSITOL SIGNALING SYSTEM
EPITHELIAL CELL SIGNALING IN HELICOBACTER PYLORI INFECTION
LYSOSOME
VALINE LEUCINE AND ISOLEUCINE DEGRADATION
BETA ALANINE METABOLISM
STEROID HORMONE BIOSYNTHESIS
RETINOL METABOLISM
GLYCOLYSIS GLUCONEOGENESIS
HUNTINGTONS DISEASE
LEUKOCYTE TRANSENDOTHELIAL MIGRATION
BUTANOATE METABOLISM
NICOTINATE AND NICOTINAMIDE METABOLISM
ALDOSTERONE REGULATED SODIUM REABSORPTION
METABOLISM OF XENOBIOTICS BY CYTOCHROME P450
ALZHEIMERS DISEASE
PROGESTERONE MEDIATED OOCYTE MATURATION
VASOPRESSIN REGULATED WATER REABSORPTION
SPLICEOSOME
ARGININE AND PROLINE METABOLISM
GLYCOSAMINOGLYCAN BIOSYNTHESIS HEPARAN SULFATE
PROTEASOME
BASE EXCISION REPAIR
MISMATCH REPAIR
DNA REPLICATION
PRION DISEASES
STEROID BIOSYNTHESIS
CELL CYCLE
HOMOLOGOUS RECOMBINATION
N GLYCAN BIOSYNTHESIS
PROTEIN EXPORT
NES
d
UP
No Change
DOWN
SPF
vs
GF
Regulatory Clusters
Opposite
None
Core-ATF6 UP
Core-ATF6 DOWN
GF UP
GF DOWN
SPF UP
SPF DOWN
% Genes in flow
0.04%
84.70%
2.65%
0.75%
0.87%
0.79%
5.93%
4.27%
Number of genes
e
CORE-ATF6 UP
-Log10p.adj
Log2FC
f
SPF UP
-Log10p.adj
Log2FC
g
Acute nATF6 Vil-CreERT2Tg SPF
-Log10p.adj
Log2FC
DOWN (733 genes, 5.29%)
No Change (12208 genes, 88.11%)
UP (913 genes, 6.59%)

Fig.4

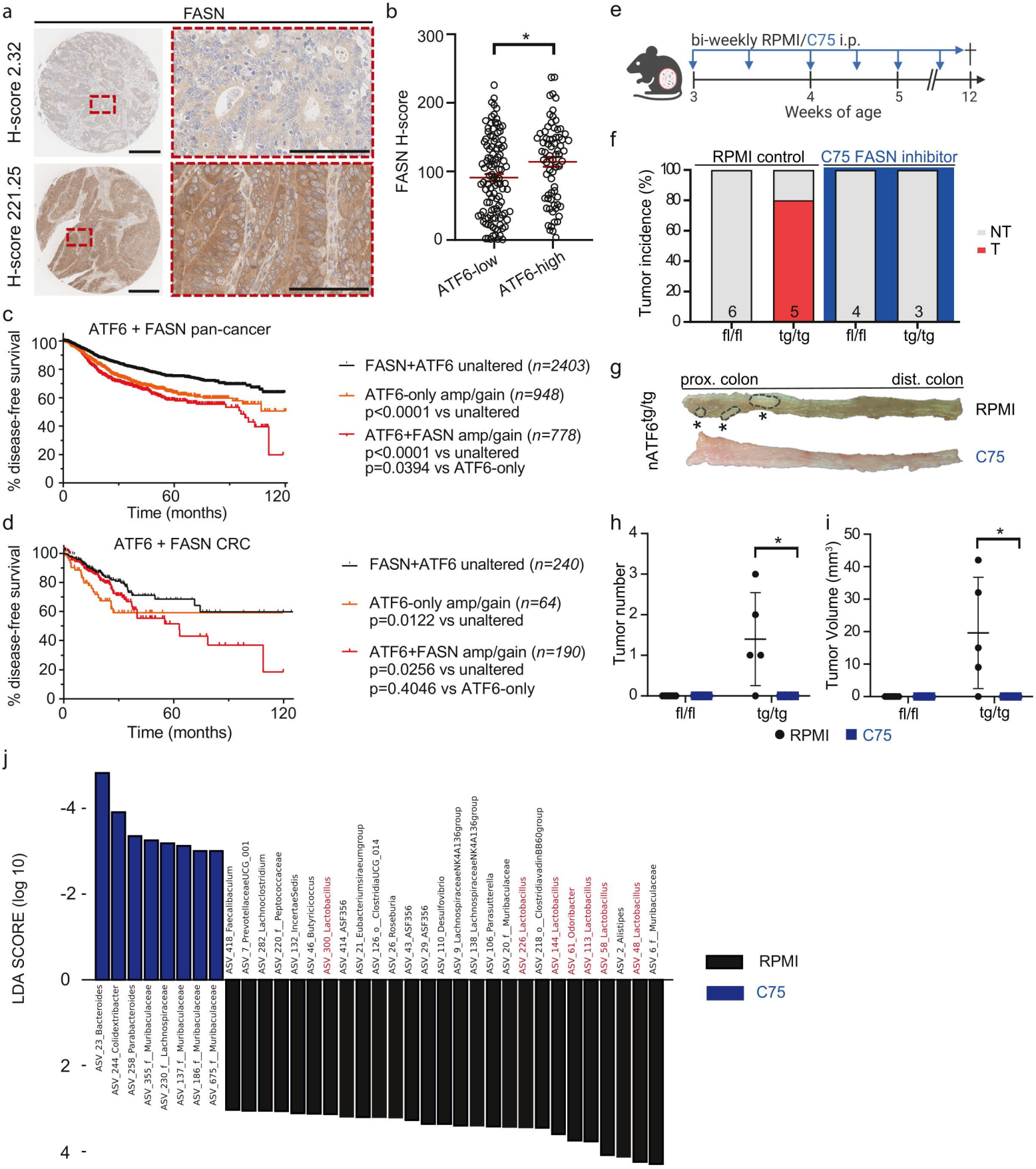
a
FASN
H-score 2.32
H-score 221.25
b
FASN H-score
300
200
100
0
*
ATF6-low
ATF6-high
e
bi-weekly RPMI/C75 i.p.
3
4
5
12
Weeks of age
f
RPMI control
C75 FASN inhibitor
Tumor incidence (%)
100
80
60
40
20
0
6
5
4
3
fl/fl
tg/tg
fl/fl
tg/tg
NT
T
c
ATF6 + FASN pan-cancer
% disease-free survival
Time (months)
0
60
120
FASN+ATF6 unaltered (n=2403)
ATF6-only amp/gain (n=948)
p<0.0001 vs unaltered
ATF6+FASN amp/gain (n=778)
p<0.0001 vs unaltered
p=0.0394 vs ATF6-only
g
prox. colon
dist. colon
nATF6tg/tg
RPMI
C75
d
ATF6 + FASN CRC
% disease-free survival
Time (months)
FASN+ATF6 unaltered (n=240)
ATF6-only amp/gain (n=64)
p=0.0122 vs unaltered
ATF6+FASN amp/gain (n=190)
p=0.0256 vs unaltered
p=0.4046 vs ATF6-only
h
Tumor number
fl/fl
tg/tg
i
Tumor Volume (mm3)
fl/fl
tg/tg
RPMI
C75
j
LDA SCORE (log 10)
-4
-2
0
2
4
ASV_23_Bacteroides
ASV_244_Colidextribacter
ASV_258_Parabacteroides
ASV_355_f__Muribaculaceae
ASV_230_f__Lachnospiraceae
ASV_137_f__Muribaculaceae
ASV_186_f__Muribaculaceae
ASV_675_f__Muribaculaceae
ASV_418_Faecalibaculum
ASV_7_PrevotellaceaeUCG_001
ASV_282_Lachnoclostridium
ASV_220_f__Peptococcaceae
ASV_132_IncertaeSedis
ASV_46_Butyricicoccus
ASV_300_Lactobacillus
ASV_414_ASF356
ASV_21_Eubacteriumsiraeumgroup
ASV_126_o__ClostridiaUCG_014
ASV_26_Roseburia
ASV_43_ASF356
ASV_29_ASF356
ASV_110_Desulfovibrio
ASV_9_LachnospiraceaeNK4A136group
ASV_138_LachnospiraceaeNK4A136group
ASV_106_Parasutterella
ASV_20_f__Muribaculaceae
ASV_226_Lactobacillus
ASV_218_o__ClostridiavadinBB60group
ASV_144_Lactobacillus
ASV_61_Odoribacter
ASV_113_Lactobacillus
ASV_58_Lactobacillus
ASV_2_Alistipes
ASV_48_Lactobacillus
ASV_6_f__Muribaculaceae
RPMI
C75

Fig. 5

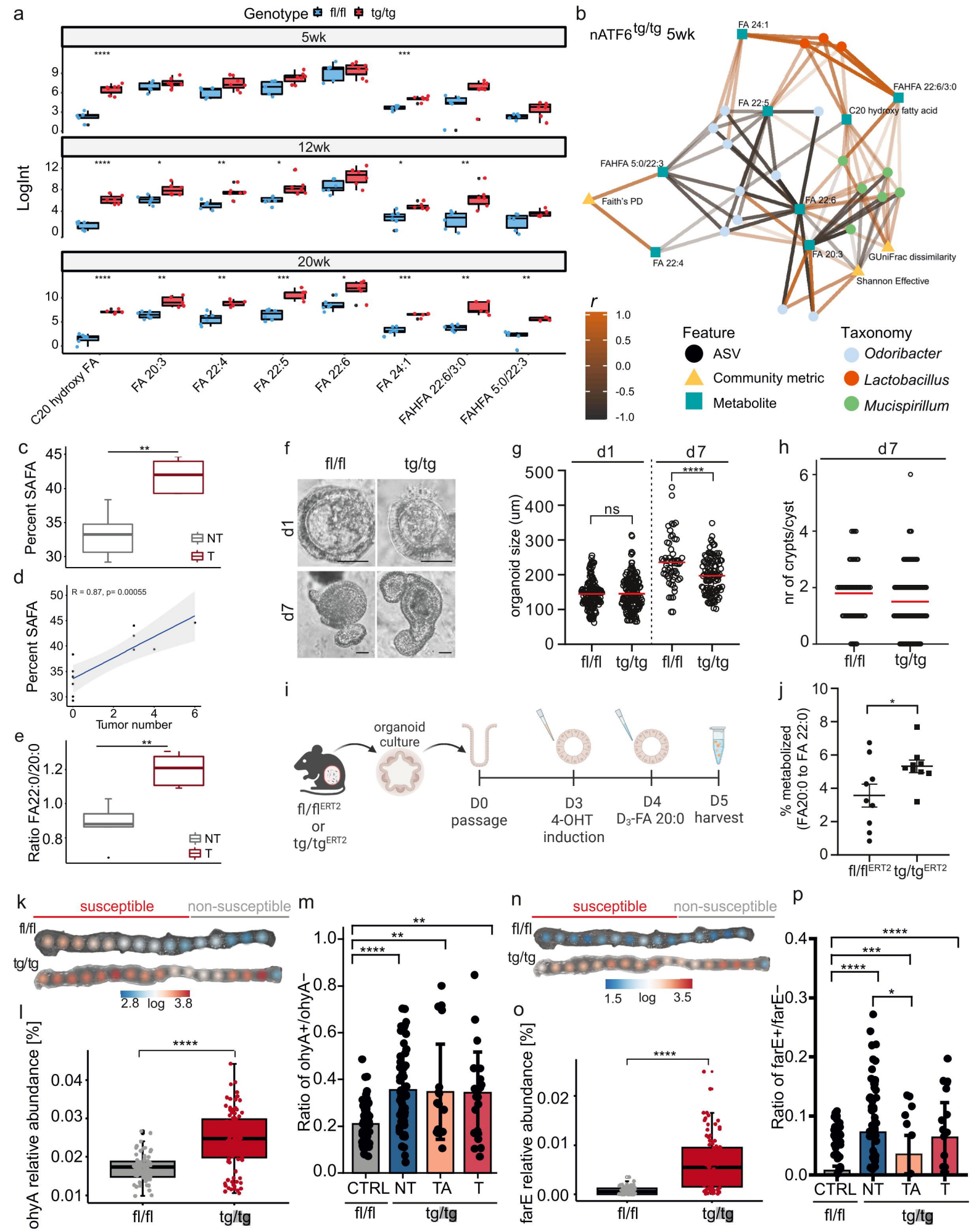
a
Genotype fl/fl tg/tg
5wk
12wk
20wk
LogInt
C20 hydroxy FA
FA 20:3
FA 22:4
FA 22:5
FA 22:6
FA 24:1
FAHFA 22:6/3:0
FAHFA 5:0/22:3
b
nATF6tg/tg 5wk
FA 24:1
FAHFA 22:6/3:0
FA 22:5
C20 hydroxy fatty acid
FAHFA 5:0/22:3
Faith's PD
FA 22:6
FA 22:4
FA 20:3
GUniFrac dissimilarity
Shannon Effective
r
Feature
ASV
Community metric
Metabolite
Taxonomy
Odoribacter
Lactobacillus
Mucispirillum
c
Percent SAFA
NT
T
d
R = 0.87, p= 0.00055
Percent SAFA
Tumor number
e
Ratio FA22:0/20:0
NT
T
f
fl/fl
tg/tg
d1
d7
g
d1
d7
organoid size (um)
ns
fl/fl
tg/tg
h
d7
nr of crypts/cyst
fl/fl
tg/tg
i
organoid culture
fl/flERT2 or tg/tgERT2
D0 passage
D3 4-OHT induction
D4 D3-FA 20:0
D5 harvest
j
% metabolized (FA20:0 to FA 22:0)
fl/flERT2
tg/tgERT2
k
susceptible
non-susceptible
fl/fl
tg/tg
2.8 log 3.8
l
ohyA relative abundance [%]
fl/fl
tg/tg
m
Ratio of ohyA+/ohyA−
CTRL
NT
TA
T
fl/fl
tg/tg
n
susceptible
non-susceptible
fl/fl
tg/tg
1.5 log 3.5
o
farE relative abundance [%]
fl/fl
tg/tg
p
Ratio of farE+/farE−
CTRL
NT
TA
T
fl/fl
tg/tg